Catalytic Production of δ-Valerolactone (DVL) from Biobased 2-Hydroxytetrahydropyran (HTHP) – Combined Experimental and Modeling Study

Raka G. Dastidar,[1,2] Javier E. Chavarrio,[1] Zhen Jiang,[1] Daniel J. McClelland,[2] Manos Mavrikakis,[1] George W. Huber[1,*]

[1]Department of Chemical and Biological Engineering, University of Wisconsin-Madison, Madison, Wisconsin 53706, USA
[2]Pyran, Inc., 505 South Rosa Road, Suite 112, Madison, Wisconsin 53719, USA
*Corresponding author: gwhuber@wisc.edu

Abstract

δ-Valerolactone (DVL) is a five-carbon (C5) cyclic ester that can undergo ring-opening polymerization to yield high-performance, biocompatible polyesters. But current market prices of C5 chemicals like DVL are very high due to poor availability of C5 feedstock in petroleum. Herein, we demonstrate a novel route to DVL synthesis via dehydrogenation of biomass-derived 2-hydroxytetrahydropyran (HTHP) over Cu/SiO_2 without the use of toxic reagents. Since HTHP exists in thermal equilibrium with 3,4-dihydropyran (DHP) via dehydration, and with 2,2'-oxybis(tetrahydropyran) and 5-(tetrahydropyran-2-yloxy)pentanal via acetalization, we have also determined the thermochemistry (ΔH_{rxn} and ΔG_{rxn}) of each competing reaction using density functional theory (DFT) calculations at the M06-2X/cc-pVTZ level. Lastly, by developing a kinetic model of all 8 reactions involved, we have achieved 84% selectivity to DVL at 150°C in a packed bed reactor for over 72 hours of time on stream.

Introduction

Global demand for high-performance polymers from the biomedical and pharmaceutical industries is projected to exceed USD 54 billion by 2027.[1] δ-Valerolactone (DVL) is a five-carbon (C5) cyclic ester capable of undergoing ring-opening polymerization to poly(δ-valerolactone) (PVL) – a biocompatible polyester that exhibits very high tensile strength and fracture strain, markedly outperforming commodity plastics like high density polyethylene (HDPE).[2] Lactone-based polymers like PVL also have the unique property of *in vivo* biodegradation into nontoxic metabolites (lactic acid, CO_2, and water) via hydrolysis of their ester backbone,[3, 4] enabling their use in bone grafts,[5] tissue engineering scaffolds,[6] and implantable drug delivery systems (IDDS).[7] Furthermore, PVL is chemically recyclable – depolymerizing PVL with an acid catalyst at 100°C yields DVL in quantitative yields with no loss in the properties of recycled PVL after 5 cycles – facilitating closed loop PVL manufacturing.[8] Other bio-based C5 lactones include γ-valerolactone (GVL) and α-angelica lactone (AGL), which are produced from intramolecular esterification of 4-hydroxypentanoic acid and acid-catalyzed dehydration of levulinic acid, respectively.[9, 10] While GVL is mainly used as a green solvent, AGL is used in fragrances and pharmaceuticals.

Current market prices of C5 monomers like DVL are considerably higher than their C4 or C6 analogs due to the lack of readily accessible C5 feedstock in petroleum.[11] **Scheme 1** elucidates the fossil-based routes for the synthesis of DVL, butyrolactone, and caprolactone. Industrially, most butyrolactone is produced from dehydrogenation of 1,4-butanediol,[12] which is made from acetylene and formaldehyde via the Reppe process.[13] Caprolactone and DVL are prepared from the Baeyer-Villiger oxidation of cyclohexanone and cyclopentanone, respectively, using peroxides.[14] While the market size of cyclohexanone in 2022 was a staggering USD 8.3 billion, the market size of cyclopentanone was significantly smaller at USD 128 million.[15] The difference lies in the number and complexity of reagents needed to produce each compound. Cyclohexanone is extracted from the ketone-alcohol oil (KA Oil) mixture produced from the oxidation of cyclohexane.[16] But cyclopentanone production involves

cyclohexanone oxidation with nitric acid in a multi-step reaction with NO_x byproducts,[17] then ketonic decarboxylation of the resulting adipic acid using barium hydroxide, with 42% of the adipic acid lost to CO_2 and water.[18] DVL can also be produced by the dehydrogenation of 1,5-pentanediol,[19, 20] which is produced from the hydrogenation of glutaric acid, a byproduct of adipic acid manufacturing.[21] Irrespective of the route chosen, DVL production from fossil feedstocks is extremely hazardous and expensive.

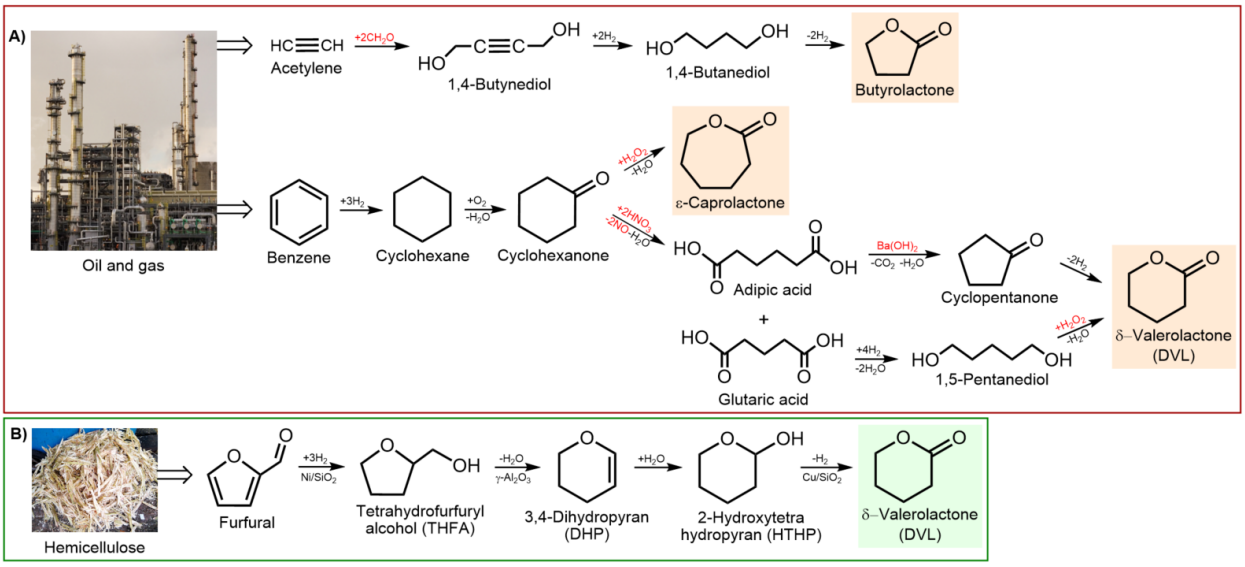

Scheme 1. Lactone production routes and their associated feedstocks: **A**) Fossil-based routes for the production of butyrolactone, caprolactone, and δ-valerolactone (DVL). **B)** Proposed biomass-derived route for the production of DVL (this work). Reagents in red are toxic and/or corrosive.

Herein, we demonstrate a novel route to DVL production via dehydrogenation of biobased 2-hydroxytetrahydropyran (HTHP) over Earth-abundant Cu catalysts without the use of toxic reagents (**Scheme 1)**. Unlike petroleum, lignocellulosic biomass is rich in C5 feedstock like xylose – the second most abundant sugar present in nature.[22] Xylose dehydration is carried out for the production of furfural, with the furfural market projected to exceed 400,000 MT by 2024.[23] Our group has previously demonstrated a 2-step pathway from furfural-derived THFA to HTHP: i) Dehydration and Wagner-Meerwein rearrangement of THFA to 3,4-dihydropyran (DHP);[24] and ii) Hydration of DHP to HTHP.[25] HTHP is an emerging platform chemical for the production of several C5 polymer precursors, including 1,5-pentanediol (PDO)[26] and 5-amino-1-pentanol.[27] Pyran, Inc. has successfully piloted this technology and produced ton quantities of polymer grade PDO.[28] Our research team has also shown that PDO production from hydrogenation of HTHP, as opposed to the fossil route shown in **Scheme 1A**, leads to 95% reduction in greenhouse gas (GHG) emissions and 40-50% drop in the minimum selling price of PDO.[29] However, the thermochemistry of HTHP, and the kinetics of DVL formation and degradation remain unknown.

This work is the first to screen numerous metal oxide and supported-metal catalysts for DVL production from HTHP dehydrogenation. Since HTHP is in thermal equilibrium with DHP, 5-hydroxypentanal (5-HP), 2,2'-oxybis(tetrahydropyran) (Dimer 1; D1), and 5-(tetrahydropyran-2-yloxy)pentanal (Dimer 2; D2),[25] we have also determined the thermochemistry of each competing equilibrium using density functional theory (DFT) calculations at the M06-2X/cc-pVTZ level of theory. Next, we evaluated the rate constants, apparent activation energies (E_a), and reaction orders using a

tubular flow reactor at varying temperatures, contact times, and HTHP partial pressures (P_{HTHP}). Furthermore, we developed a kinetic model to predict the selectivity to DVL as a function of both temperature and contact time, wherein the forward (k_f) and backward (k_b) rate constants are scaled with respect to temperature using the Arrhenius relation and DFT-calculated equilibrium rate constants (K_{eq}), respectively. Lastly, we experimentally verified the model-predicted DVL selectivity by carrying out HTHP dehydrogenation to DVL for 72 hours at the optimized reaction conditions. Our findings establish the catalytic dehydrogenation of furfural-derived HTHP as a novel route to DVL synthesis, and provide directions for reactor design to control the selectivity to DVL by minimizing side reactions.

Experimental Section

Materials: 3,4-Dihydropyran (Fisher Scientific, 99%), 2-hydroxytetrahydropyran (Acros Organics, 97%), δ-valerolactone (VWR International, 99%), 1,5-pentanediol (Thermo Scientific, 98%), tetrahydropyran (Sigma-Aldrich, 99%), Argon (Airgas, UHP grade), H_2 (Airgas, UHP grade), $Cu(NO_3)_2{\cdot}3H_2O$ (Sigma Aldrich), $Ni(NO_3)_2{\cdot}6H_2O$ (Fisher Scientific), SiO_2 (Sigma Aldrich, 4-20 mesh), Al_2O_3 (Santa Cruz Biotechnology), MgO (Santa Cruz Biotechnology), 5 wt% Pd/SiO_2 (VWR International), and 5 wt% Pt/SiO_2 (Sigma Aldrich) were used as received.

Catalyst synthesis and characterization: SiO_2, Al_2O_3 and MgO were dried at 110°C overnight in an air oven. Cu and Ni-containing catalysts with 10 wt% metal loadings were synthesized using incipient wetness impregnation, wherein the desired metal nitrate salt is added drop-wise to the support and the resulting paste is mixed well, dried at 110°C overnight in an air oven, then calcined at 460°C in a muffle furnace (Thermo Fisher Thermolyne). BET surface area, pore volume, and pore width of the catalysts was measured using N_2 physisorption in a Micromeritics ASAP 2020 instrument. Temperature-programmed reduction (TPR) of the catalysts was carried out using a Micromeritics Autochem II instrument. Metal dispersion of Cu catalysts was measured in the Autochem by first reducing the catalyst at 450°C in H_2 flow, then oxidizing the Cu sites using N_2O pulse chemisorption at 90°C where the following reaction occurs: $2Cu^0 + N_2O \rightarrow Cu_2O + N_2$. Acid site density was measured using NH_3 temperature-programmed desorption (TPD), while base site density was measured using CO_2 TPD in the Autochem. Thermogravimetric analysis (TGA) was carried out in a TA Instruments TGA Q500 V6 instrument, wherein 10 mg of the catalyst was placed into a platinum pan, inserted into the instrument, then analyzed with 50 mL/min of the sample gas (N_2 or O_2) while heating from 25 to 600°C at 10°C/min. Elemental analysis was carried out using inductively coupled plasma-optical emission spectroscopy (Varian ICP-OES Vista Pro).

Batch reactor studies: Batch experiments were carried out in 45 mL Hastelloy C-276 reactor vessels (Parr Instrument Company), with each reactor head equipped with a PTFE flat gasket, K-type thermocouple, pressure transducer, safety rupture disk, manual inlet valve, exhaust valve, and dip tube. For experiments with catalysts containing transition metals: catalysts were loaded into tubular reactors and reduced *in situ* at the required temperature in 50 mL/min of H_2 flow, then flushed and sealed under Ar atmosphere, transferred to a glovebox, and 0.1 g of each catalyst was added to the batch reactor vessel without exposure to air. Pt and Pd catalysts were reduced at 100°C, while Cu and Ni catalysts were reduced at 350 and 450°C, respectively. All reductions were carried out at a heating rate of 5°C/min with a 4 h hold at the reduction temperature. After addition of the desired liquid feed and a magnetic stir bar (Fisherbrand Octagon Spinbar, PTFE-coated), the reactors were sealed with 6 compression bolts, weighed, purged with Ar 3 times, then pressurized to 200 psi with Ar. Stirring was set to 800 RPM, and the reactor temperature was raised to the desired temperature under PID control. Liquid-phase products were collected *in situ* through the dip tube, then filtered through 0.2 μm syringe filters (Thermo

Scientific) before analysis. At the end of each experiment, the reactors were quenched in ice baths, depressurized, and re-weighed.

Continuous flow reactor studies: HTHP dehydrogenation to DVL was carried out in a fixed bed reactor consisting of stainless steel tubing (15" length, ¼" O.D.) placed inside an aluminum heating block, which was then inserted into a programmable clamshell furnace (Thermo Fisher Lindberg Blue M). Reactor tubes were packed with the desired mass of catalyst, with the catalyst bed in the center of the tube (<0.5" catalyst bed height) held in place using glass beads and quartz wool on both ends. Supported-metal catalysts were reduced *in situ* in 100 mL/min H_2 at the desired temperature (specified above) for 4 hours, then flushed with Ar and heated/cooled to the reaction temperature before each experiment. Liquid feed was pumped in using an HPLC pump (Eldex Optos Series) and Ar was co-fed using a mass flow controller (Brooks 5850E Series). Reactor pressure was maintained at 200 psi using a spring-loaded back pressure regulator (Swagelok). Products were collected in a chilled cylindrical vessel maintained at 0°C with a circulating water/ethylene glycol bath. Liquid products were sampled from the bottom of the collection vessel.

Product analysis: Liquid products were identified using a quadrupole gas chromatograph-mass spectrometer (Shimadzu GCMS-QP2010) and quantified using a Shimadzu GC-2010 equipped with a flame ionization detector (FID). Both GCs are fitted with RTX-VMS columns (Restek, 30 m long, 0.25 mm I.D., 1.4 μm film thickness). External calibrations with known standards were carried out to quantify HTHP, DVL, DHP, and PDO. D1 and D2 were calibrated using a GC response factor half that of HTHP. D1 exists as two stereoisomers (*R,R* and *R,S*) which are seen as two distinct peaks with GC-FID, hence D1 concentrations have been reported as the sum of both peak areas. 5-HP is not seen as a separate peak with GC-FID as it is rapidly equilibrated with HTHP over the GC column; instead, HTHP/5-HP is quantified as as a single species. **Equations (1)** – **(3)** are used to calculate the product rate, turnover frequency (TOF), and product selectivity, respectively, for DVL, DHP, D1, and D2. The amount of Cu in the catalyst used in TOF calculations was determined using N_2O pulse chemisorption. **Equations (4) – (7)** are used to calculate HTHP conversion, carbon balance, contact time, and apparent activation energy. Humins have been quantified from the carbon balance as the difference between the moles of carbon in the feed and product.

$$\text{Product rate } (\text{min}^{-1}) = \frac{\text{mmol}_{\text{product}}}{\text{L}_{\text{solution}} \cdot \text{min}} \quad \textbf{(1)}$$

$$\text{Turnover frequency } (\text{min}^{-1}) = \frac{\text{mmol}_{\text{product}}}{\text{mL}_{\text{solution}}} \cdot \frac{\text{mL}_{\text{feed}}}{\text{min}} \cdot \frac{1}{\text{mmol}_{\text{Cu}}} \quad \textbf{(2)}$$

$$\text{Product selectivity} = \frac{\text{mmol}_{\text{product}}}{\sum \text{mmol}_{\text{product}}} \times 100\% \quad \textbf{(3)}$$

$$\text{Conversion of HTHP } (\%) = \frac{\text{mmol}_{\text{HTHP,inlet}} - \text{mmol}_{\text{HTHP,outlet}}}{\text{mmol}_{\text{HTHP,inlet}}} \times 100\% \quad \textbf{(4)}$$

$$\text{Carbon balance } (\%) = \left(\frac{\text{mmol}_{\text{Carbon,outlet}}}{\text{mmol}_{\text{Carbon,inlet}}}\right) \times 100\% \quad \textbf{(5)}$$

$$\text{Contact time } (\text{min}) = \frac{\text{g}_{\text{catalyst}}}{\text{g}_{\text{feed}}/\text{min}} \quad \textbf{(6)}$$

$$\text{Apparent activation energy, } \text{E}_\text{a}\ (\text{kJ mol}^{-1}) = (\ln \text{A} - \ln \text{k}) \cdot \text{RT} \quad \textbf{(7)}$$

Electronic Structure Calculations and Conformation Search: The step-wise work flow for density functional theory (DFT) calculations has been shown in **Figure S1**. Initial optimizations for the conformers of each molecule were first performed at the ωB97x-D[30]/6-31G* level of theory.[31, 32] For cyclic molecules (HTHP, DHP, DVL, and D1), internal torsions within the rings were explored manually. For linear molecules (5-HP and PDO), torsions were investigated in the VEGA ZZ software[33] through systematic rotations of 120°, yielding a total of 3^n potential conformers for each case, where *n* is the

number of dihedral angles in the linear chain. For D2, a screening of the lowest energy conformations was carried out in Avogadro,[34, 35] then optimized with the MMFF94 force field (FF) due to the FF's ability to predict hydrogen bonds.[36] For every successfully converged configuration, further calculations at the M06-2X/cc-pVTZ[37, 38] level of theory were performed with an ultrafine grid to optimize and characterize the stationary points of the potential energy surface (PES) using the Gaussian09 software.[39] Vibrational frequencies were corrected by using a scale factor of 0.955 to account for anharmonicity in torsional modes.[40] Subsequently, Zero Point Energy (ZPE) corrected energies were calculated for each conformer before doing thermochemistry calculations for enthalpy and Gibb's free energy. Optimized geometries of each compound are provided as a '.txt' file in the **Supporting Information**. The thermal distribution of the conformers was computed through the Boltzmann distribution as presented in **Equation (7)**, where p_i is the probability of the system being in state i, g_i is the degeneracy of energy level i, J is the total number of distinguishable conformers, $\beta = 1/k_B T$, and k_B is the Boltzmann constant.

$$p_i = \frac{g_i e^{-\beta G_i}}{\sum_{j=1}^{J} g_j e_j^{-\beta G_j}} \quad \textbf{(7)}$$

The average enthalpy and Gibbs free energy for each compound were then calculated through weighted averages as shown in **Equations (8)** and **(9)**, respectively. Gibbs free energy has an extra term known as the 'Gibbs entropy formulation' to account for the entropy increase derived from the presence of multiple conformations in the molecules.[41, 42]

$$H = \sum_{i}^{J} p_i H_i \quad \textbf{(8)}$$

$$G = \sum_{i}^{J} p_i G_i + k_B T \sum_{i}^{J} p_i ln\,(p_i) \quad \textbf{(9)}$$

Next, a set of isodesmic reactions was developed to derive the ΔH_f^o and ΔG_f^o of each compound, and to minimize the systematic error inherent to electronic structure calculations (**Table S1**). Validation of the level of theory employed in the calculations was done through comparison with experimental data when available. Heat capacities (C_P) of all the molecules in the reaction network were then computed with the 'Thermo.py' code from the NIST website by using only the global minimum energy conformation of each molecule. The predicted values of C_P were fitted to **Equation (10)**, where a and b are constants and T is in K. Subsequently, the heat of formation of each molecule at any temperature T, $\Delta H_f(T)$, was computed with **Equation (11)**, where T_{ref} is the reference temperature of 298.15 K and ΔH_f^o represents the standard heat of formation computed in the earlier steps. Free energies of formation at any temperature T, $\Delta G_f(T)$, were then calculated from the Gibbs-Helmholtz relation in **Equation (12),** where ΔG_f^o is the standard free energy of formation and $\Delta H_f(T)$ is obtained from **Equation (11)**. Lastly, the equilibrium rate constants, K_{eq}, were calculated from **Equation (13),** where ΔG_{rxn} is the difference in the free energies of the products and reactants of a given reaction at any temperature T, and R is the ideal gas constant.

$$C_p(T) = a + bT \quad \textbf{(10)}$$

$$\Delta H_f(T) = \Delta H_f^o + \int_{T_{ref}}^{T} C_p\, dT \quad \textbf{(11)}$$

$$\frac{\Delta G_f(T)}{T} = \frac{\Delta G_f^{\circ}}{T_r} - \int_{T_{ref}}^{T} \frac{\Delta H_f(T)}{T^2} dT \quad \textbf{(12)}$$

$$K_{eq}(T) = e^{-\frac{\Delta G_{rxn}(T)}{RT}} \quad \textbf{(13)}$$

Kinetic modeling: For batch reactions, rate constants were determined by solving ordinary differential equations (ODEs) in MATLAB (Version R2019B) using the 'nlinfit' function and the corresponding 95% confidence intervals were obtained using the 'nparci' function. For continuous flow reactions, rate constants were determined by the method of initial rates in the kinetic regime (<20% HTHP conversion). The heatmap of DVL selectivity as a function of temperature and contact time was obtained from Python (Version 3.10), wherein the forward and backward rate constants were scaled with temperature using the Arrhenius equation, and equilibrium rate constants (K_{eq}) were determined from DFT-calculated K_{eq}.

Results

1. Catalyst screening for HTHP dehydrogenation to DVL

HTHP is an emerging platform chemical to produce C5 chemicals, but little is known about its reactivity under inert atmosphere. Previously, *operando* temperature-variable ^{13}C NMR experiments revealed that HTHP exhibits ring-chain tautomerism to 5-hydroxypentanal (5-HP), contributing to its high reactivity.[26] In this work, HTHP conversion was analyzed in batch reactors at 150°C over various metal oxides (SiO_2, Al_2O_3, and MgO) and supported-transition metal catalysts (Cu, Ni, Pt, and Pd). The BET surface area, BJH pore volume, average pore width, metal loading, and acid/base site density of all catalysts is summarized in **Table S2**. The corresponding reaction network is shown in **Scheme 2** and the experimental results are shown in **Figure 1.** This study revealed that even in the absence of any catalysts (blank reactor), HTHP undergoes 4 reactions: i) Dehydration to 3,4-dihydropyran (DHP), ii) Acetalization to 2,2'-oxybis(tetrahydropyran) (Dimer 1; D1), iii) Acetalization to 5-(tetrahydropyran-2-yloxy)pentanal (Dimer 2; D2), and iv) Degradation to dark-colored solids (humins). Cyclic alcohols like cyclohexanol are also known to undergo dehydration to their corresponding cycloalkenes but the reaction does not proceed without catalysts, unlike HTHP dehydration to DHP.[43] The thermal reactions of HTHP were observed in stainless steel, Hastelloy, and glass reactors at nearly identical rates, indicating that the materials of construction are not catalyzing any product formation. The product rates were also unchanged as the reactor pressure was varied from 0 – 300 psi and the stirring speed was varied from 200 – 800 RPM, ruling out any mass transfer limitations.

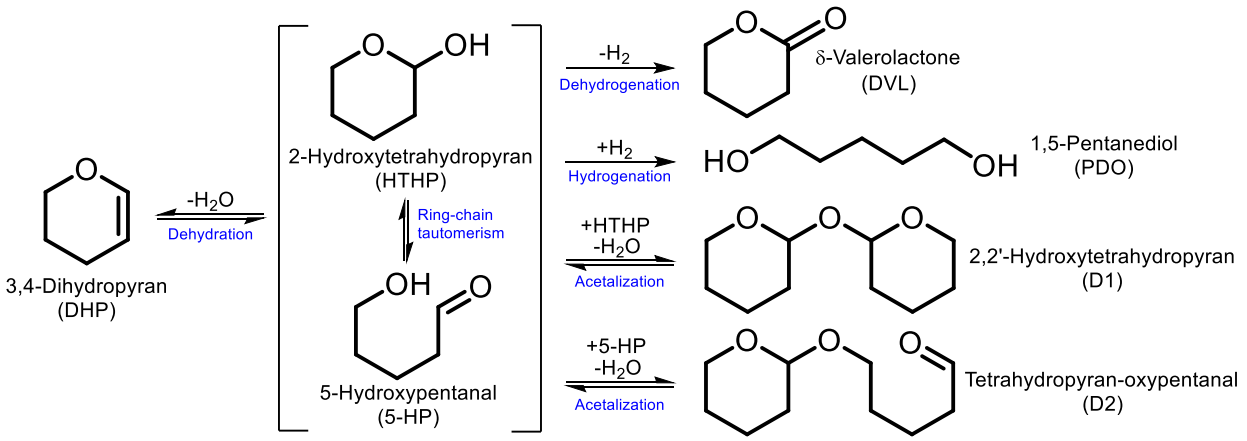

Scheme 2. Reaction network for thermocatalytic conversion of HTHP to DHP, 5-HP, DVL, PDO, D1 and D2 via dehydration, ring-chain tautomerism, dehydrogenation, hydrogenation, and acetalization reactions, respectively.

Over acidic metal oxide catalysts like SiO_2 and Al_2O_3, HTHP conversion was around 35%, with slightly higher rates of D2 and DHP formation than the blank reactor. Over a basic metal oxide catalyst like MgO, HTHP conversion dropped to 30% and humins were formed 4× faster than in the absence of catalysts. This indicates that in addition to the thermal conversion of HTHP, acid sites are catalyzing the dehydration and acetalization reactions of HTHP to produce DHP, D1, and D2, while basic sites are contributing to HTHP degradation. When a transition metal (Cu, Ni, Pt or Pd) was present in the catalyst, HTHP dehydrogenation to DVL was observed. Over CuO/SiO_2, HTHP conversion increased to 75% and DVL was produced at 0.007 mmol L^{-1} min^{-1}, albeit at lower rates than DHP (0.008 mmol L^{-1} min^{-1}) and D2 (0.01 mmol L^{-1} min^{-1}). When the catalyst was reduced *in situ* to yield Cu/SiO_2, DVL rates increased by 4× to 0.03 mmol L^{-1} min^{-1} and only a negligible amount of humins were observed. Due to the higher rate of DVL formation and lower rates of HTHP degradation to humins, all other transition metal catalysts were reduced *in situ* to yield metallic active sites. DVL production rates were observed to vary in the following order: Cu/SiO_2 > Cu/Al_2O_3 > Pt/SiO_2 > Pd/SiO_2 > CuO/SiO_2 > Ni/SiO_2 > Cu/MgO. Cu/SiO_2 has also been shown to be an excellent catalyst for cyclohexanol dehydrogenation to cyclohexanone.[44] While HTHP conversion over Pt/SiO_2 and Pd/SiO_2 was >86%, the highest out of all the catalysts studied, the DVL selectivity was lower than that over Cu/SiO_2 due to higher rates of DHP, D2, and humin formation on Pt/SiO_2 and Pd/SiO_2. HTHP hydrogenation to 1,5-pentanediol (PDO) from H_2 produced during HTHP dehydrogenation to DVL was also observed over Ni/SiO_2, Cu/Al_2O_3, Pt/SiO_2, and Pd/SiO_2, but was negligible over Cu/SiO_2. Due to its higher activity and selectivity for DVL production and suppression of humin formation, Cu/SiO_2 was used for the kinetic studies later in this work.

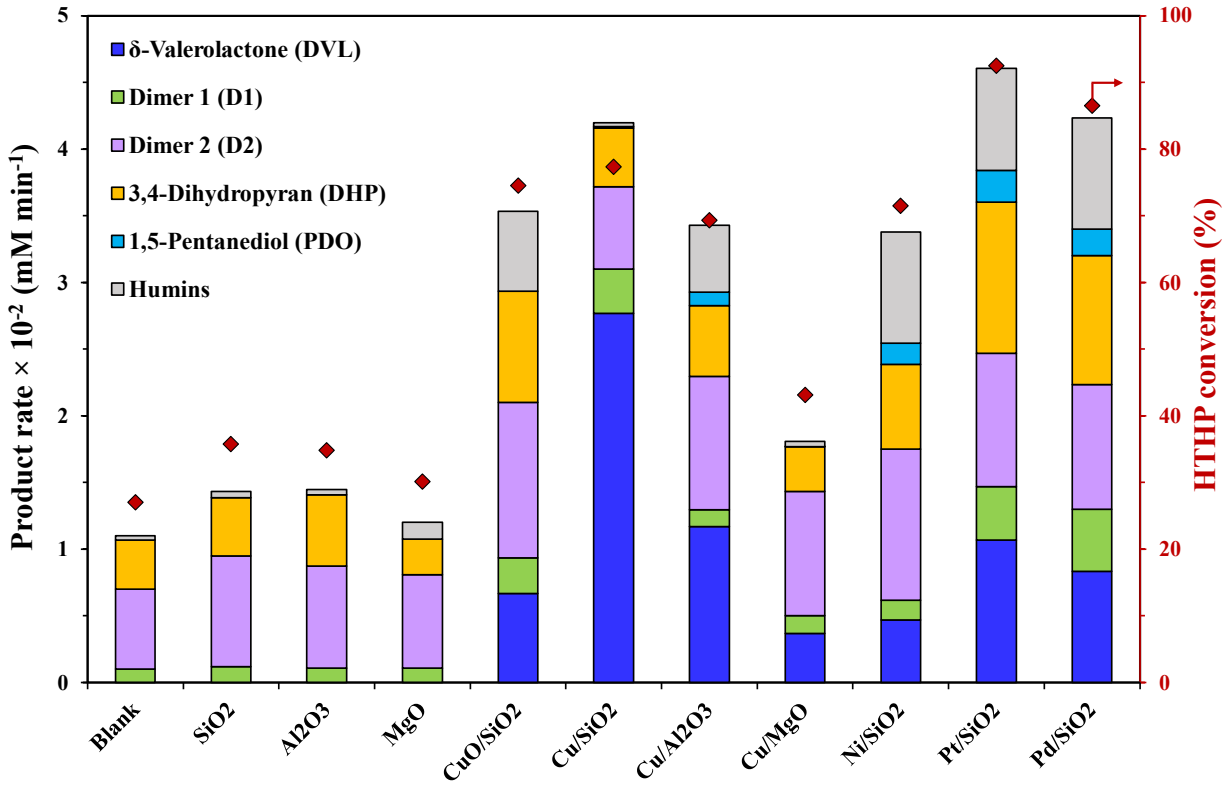

Figure 1. Product rates and HTHP conversion from thermocatalytic reactions of HTHP over various catalysts. Reaction conditions: 150°C, 2 mM HTHP in THP (feed), 100 psi Ar, 0.1 g of catalyst (if any), 45 mL Parr reactor, 800 rpm stirring, 30 min.

2. Thermal equilibrium between HTHP, DHP, D1, and D2

Experiments at varying reaction temperatures and feed compositions in the absence of any heterogeneous catalysts were carried out in batch reactors to measure the forward (k_f) and equilibrium rate constants (K_{eq}) of HTHP conversion to DHP, D1, and D2. The fitted values of k_f and K_{eq} for the six observed reactions are listed in **Table 1**. **Figure 2** shows the effect of temperature on the concentration profiles of HTHP, DHP, D1, and D2 in the absence of any heterogeneous catalysts. As the temperature was increased from 100 – 150°C, the K_{eq} for HTHP dehydration to DHP (reaction R1) increased nearly an order of magnitude from 1.6 to 15.8, while the K_{eq} for HTHP dimerization to D2 (reaction R3) increased slightly from 72.1 to 80.1. On the other hand, K_{eq} for all other reactions (R2, R4, and R5) decreased with increasing temperature. The carbon balance was ~99% at 100°C, but the formation of humins (reaction R6) was observed at T >125°C. The rate of humin formation increased monotonically with temperature, with 0.12 mM of humins produced at 150°C. While Barnett *et al.* have demonstrated that HTHP can be produced from autocatalytic hydration of DHP,[25] this study reveals that DHP, HTHP, D1, D2, and water are all in thermal equilibrium. As a result, the product mixture from HTHP dehydrogenation to DVL at 150°C also contains DHP, D1, and D2 from homogeneous reactions. As discussed in later sections, the experimentally-observed K_{eq} was compared with DFT-calculated K_{eq} and found to be in good agreement.

Table 1. Experimentally-fitted forward rate constants (k_f) and equilibrium constants (K_{eq}) of the thermal reactions between HTHP, DHP, D1, D2, and humins. Reaction conditions: 100-150°C reaction temperature, 45 mL Parr reactor, 800 rpm stirring, 100 psi Ar inert.

Reaction	**k_f ($\times 10^{-3}$) [a]**				**$K_{eq} = k_f/k_b$**			
	100°C	**125°C**	**135°C**	**150°C**	**100°C**	**125°C**	**135°C**	**150°C**
R1: HTHP → DHP + H_2O	1.2	3.6	5.6	9.3	1.6	7.1	10.5	15.8
R2: 2HTHP → D1 + H_2O	0.9	2.9	4.1	8.2	10.3	6.2	3.9	4.8
R3: 2HTHP → D2 + H_2O	2.3	7.9	11.8	23.1	72.1	78	78.2	80.1
R4: HTHP + DHP → D1	0.9	2.2	3.4	4.9	4.8	1.1	0.5	0.2
R5: HTHP + DHP → D2	1.6	4.3	5.9	10.3	45.5	12.1	6.8	4.1
R6: HTHP → Humins	0.1	0.6	1.2	2.5	-	-	-	-

a: The u nits of k_f are: min^{-1} for R1, $L\ mmol^{-1}\ min^{-1}$ for R2, R3, and R6, and $L^2\ mmol^{-2}\ min^{-1}$ for R4 – R5.

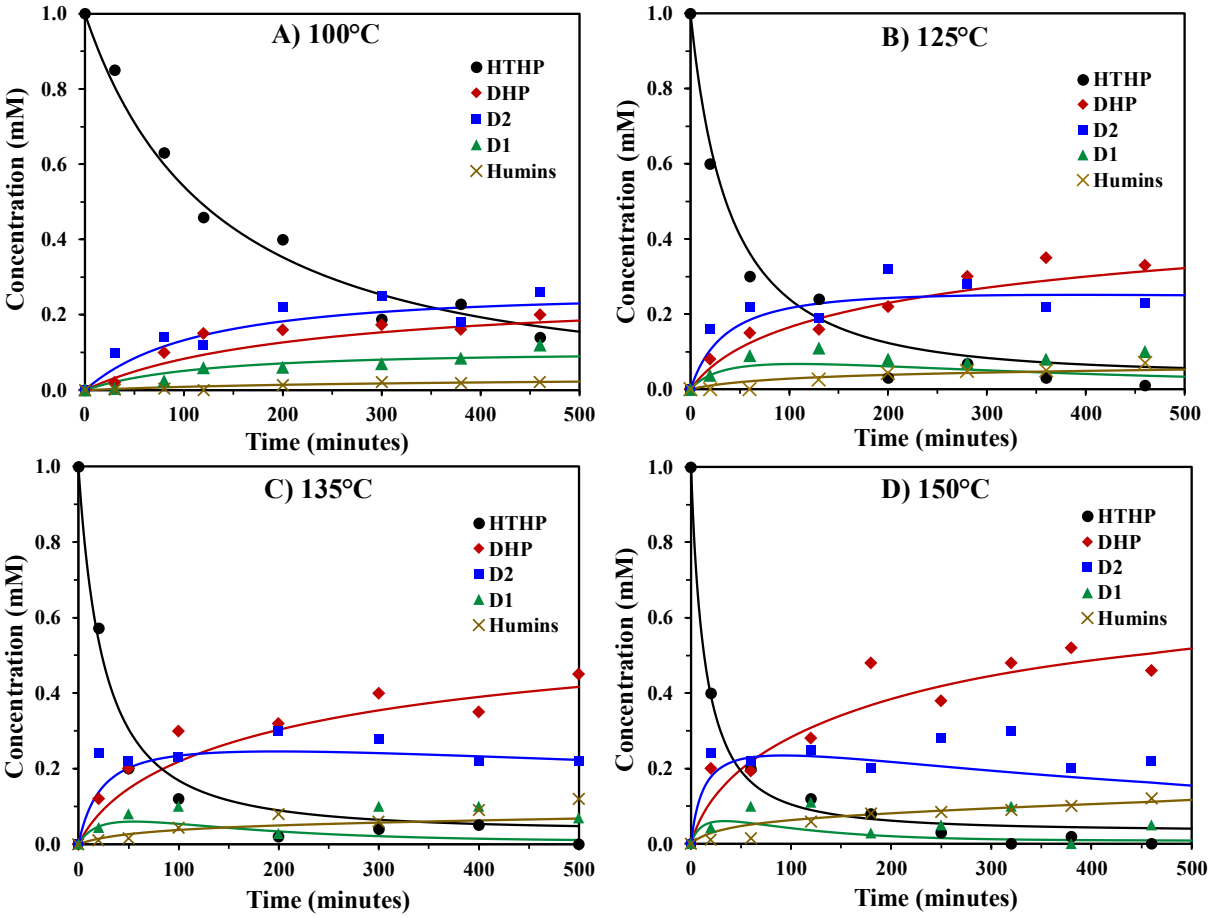

Figure 2. Effect of temperature on the thermal equilibrium between HTHP, DHP, D1, and D2 at: **A)** 100°C, **B)** 125°C, **C)** 135°C, and **D)** 150°C. Reaction conditions: varying temperatures, 1 mM HTHP in THP (feed), 100 psi Ar, 45 mL Parr reactor, 800 rpm stirring, 500 min. Solid lines are model-predicted values.

Next, experiments with variable feed compositions of HTHP and DHP were carried out to determine if D1 and D2 are formed from two molecules of HTHP dimerizing (reactions R2 and R3) or from DHP acetalizing with HTHP (reactions R4 and R5), or a combination of both. The results of the co-feed experiments are shown in **Figure 3.** No products were observed when the feed was pure DHP in the absence of HTHP or water. When the feed consisted of 0.1 mM HTHP, DHP was the major product (0.06 mM) after 500 minutes. As the feed concentration was increased to 2 mM HTHP, D2 was the major product (0.6 mM) within 350 minutes. Co-feed experiments with varying amounts of HTHP and DHP in the feed resulted in DHP being the major component in the product mixture, followed by D2 then D1. The fitted model based on varying HTHP concentrations reveals that HTHP dehydration and humin formation are both 1st order in HTHP concentration, while HTHP acetalization to D1 and D2 is 2nd order. This study further reveals that D1 and D2 are produced from four different reactions: HTHP dimerization (R2 and R3) and DHP acetalizing with HTHP (R4 and R5), with HTHP dimerization contributing at higher rates.

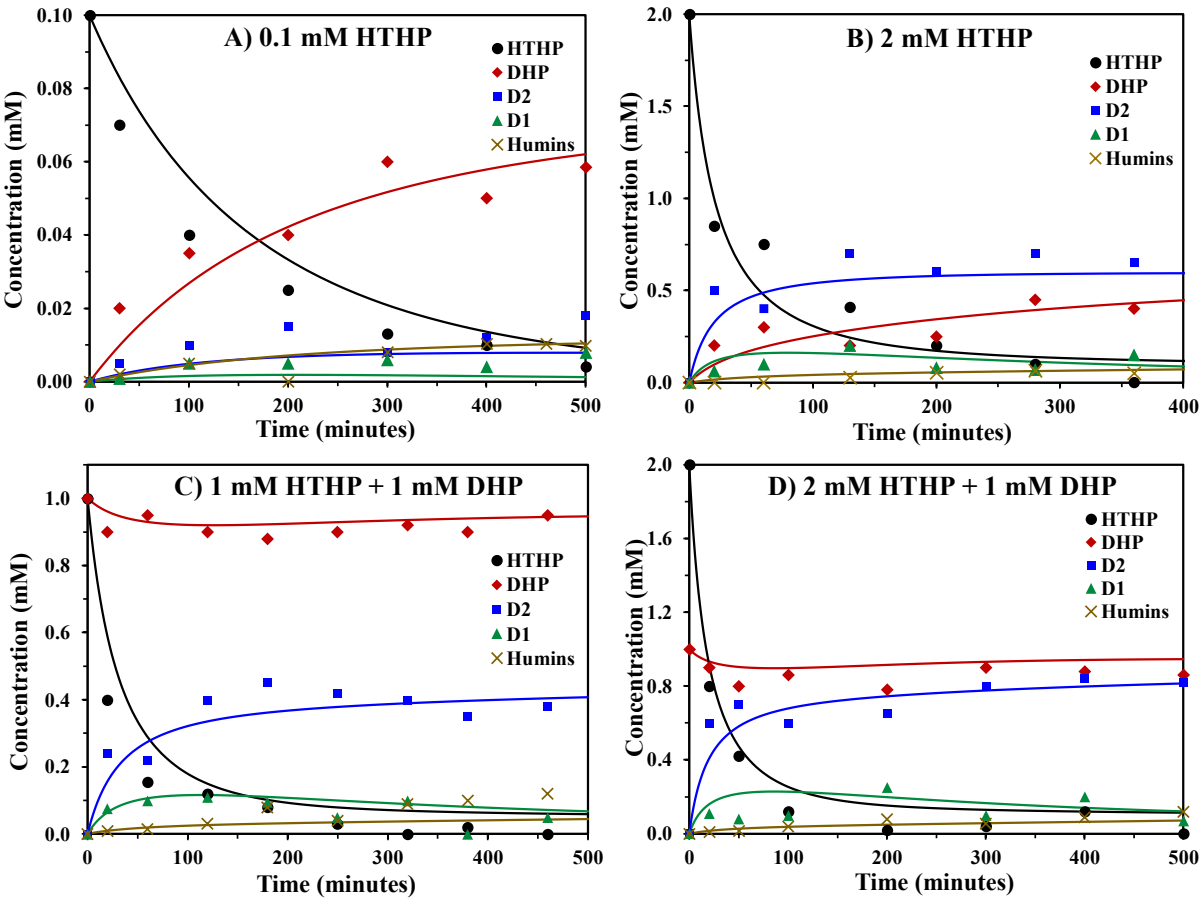

Figure 3. Effect of feed composition on the thermal equilibrium between HTHP, DHP, D1 and D2 for the following feeds: **A)** 0.1 mM HTHP, **B)** 2 mM HTHP, **C)** 2 mM HTHP + 1 mM DHP, and **D)** 1 mM HTHP + 1 mM DHP. Reaction conditions: 125 °C, 45 mL Parr reactor, varying concentrations of HTHP/DHP in THP (feed), 800 rpm stirring, 100 psi Ar. Solid lines are model-predicted values.

3. DVL stability study

The thermal reactivity of DVL in an inert atmosphere was studied in batch reactors to determine if DVL undergoes degradation and/or is in equilibrium with any compounds. When DVL was heated up from 125 – 175°C, dark-colored solids were observed at the bottom of the reactor from humin formation (**Figure 4**). No other compounds were observed with GC-MS. DVL degraded to humins at a first-order degradation rate (k_d) of 0.0001 mmol L^{-1} min^{-1} at 125°C, which increased to 0.0004 mmol L^{-1} min^{-1} at 150°C, and 0.0014 mmol L^{-1} min^{-1} at 175°C. The apparent activation energy of DVL degradation is found to be 78.9 ± 0.2 kJ mol^{-1}.

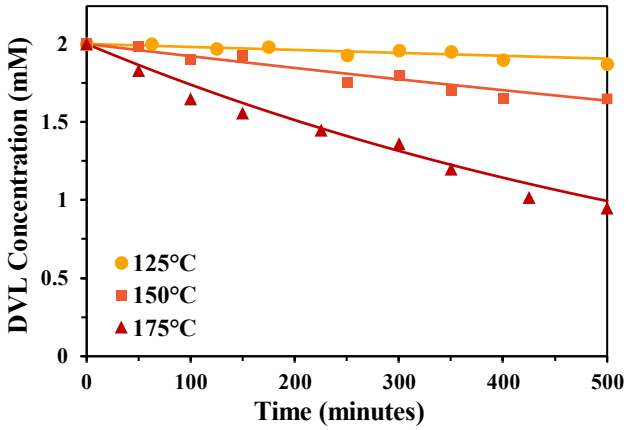

Figure 4. Effect of reaction temperature on DVL degradation to humins. Reaction conditions: 2 mM DVL in THP, 45 mL Parr reactor, 800 rpm stirring, 100 psi Ar. Solid lines are model-predicted values.

4. Reaction mechanism for the thermal equilibrium between HTHP, DHP, D1 and D2

Based on the kinetic studies carried out, the proposed reaction mechanism for the thermal equilibrium between HTHP, 5-HP, DHP, D1, and D2 is shown in **Scheme 3**. Ring-chain tautomerism of HTHP leads to 5-HP formation via intramolecular proton transfer between the ether and hydroxyl oxygen atoms. The rapid interconversion between the ring-open and ring-closed tautomers contributes to the high reactivity of the [HTHP/5-HP] feed. HTHP can also undergo protonation at the hydroxyl oxygen followed by dehydration to form a carbocation intermediate, which is resonance-stabilized by the ether oxygen donating one of its lone pair of electrons to form a C=O bond within the ring. The proposed carbocation intermediate can then undergo 2 competing pathways: i) Deprotonation and C=C bond formation to produce DHP, or ii) Acetalization to D1 (or D2) by addition of HTHP (or 5-HP) and deprotonation at the central oxygen atom. When carrying out DHP hydration with water to produce HTHP (or when HTHP is co-fed with DHP), the vinyl carbon of DHP can abstract a proton from the feed mixture and re-form the carbocation intermediate, leading to the establishment of an equilibrium between DHP, HTHP, D1 and D2 once again. However, pure DHP in the absence of a proton source does not react to form any products thermally.

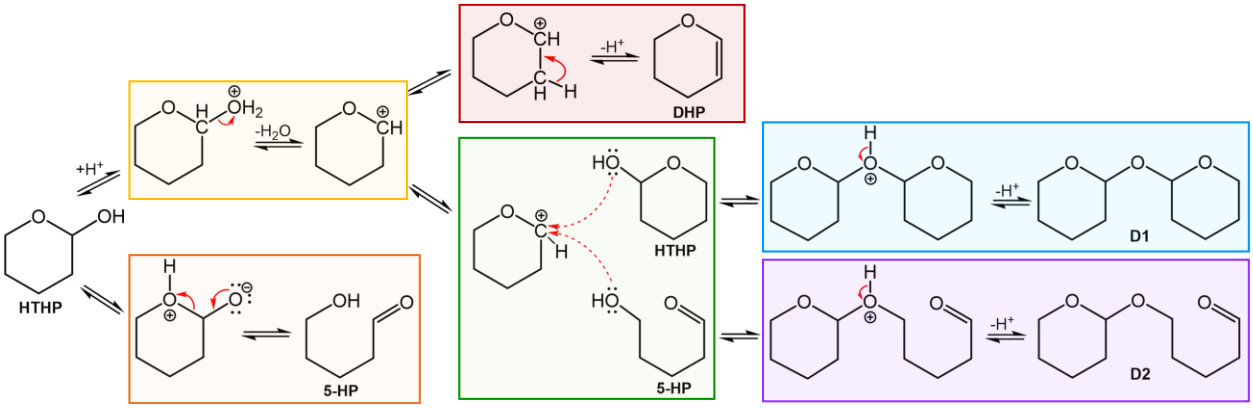

Scheme 3. Proposed reaction mechanism for thermal equilibrium between HTHP, DHP, D1 and D2, including ring-chain tautomerism to 5-HP (orange), formation of a common carbocation intermediate (yellow), deprotonation to DHP (red), acetalization of the carbocation intermediate with HTHP or 5-HP (green), and subsequent formation of D1 (blue) or D2 (purple).

3) Thermochemistry from DFT calculations

To better understand the equilibrium pathway for HTHP conversion to DHP, D1, and D2 products, we performed a systematic *ab initio* thermodynamic study of the reactions shown in **Scheme 1**, while the calculation workflow can be found in **Figure S1**. First, the lowest energy conformers of HTHP, 5-HP, DHP, DVL, PDO, D1, and D2 were obtained (**Table 2).** The conformational search for HTHP was guided by modifying the well-known cyclohexanol conformers,[45] owing to the structural similarity of both cyclic alcohols. The results show that the chair configuration of HTHP with the -OH group in the axial position is the potential energy global minimum (**Table 2A**). Two other chair configurations of HTHP with the -OH group in equatorial positions were located at 3.7 and 6.2 kJ mol^{-1} with respect to its global minimum. Our finding is in good agreement with Tvaroska *et al.*, where the other two chair configurations of HTHP with equatorial-OH were also reported to be energetically metastable with 3.3 and 5.8 kJ mol^{-1} larger than the axial-OH configuration from ACM/tzvp[46] calculations.

Next, the conformers of 5-HP were investigated and its global minimum potential energy conformer was observed due to the internal hydrogen bonds (**Table 2B**). At least 19 other conformations were found with stability for the relative energy less than 8.3 kJ mol^{-1} compared with the global minimum at room temperature. Notably, DHP was found to have only two isoenergetic conformations (specular images), adopting the half-chair configuration (**Table 2C**). The presence of the oxygen atom and double bond in position 2-3 offers stiffness and hinders the formation of other conformers, contrary to the case of its analogous hydrocarbon, cyclohexene. Previous theoretical work by Ghosh *et al.* yielded the same conformer.[47]

The ground state configuratation of DVL was found to adopt the half-chair configuration (**Table 2D**). Raman spectroscopy has showed that the half-chair and boat conformations are separated by 2.5 kJ mol^{-1} at room temperature,[48] which is in agreement with this work (2.55 kJ mol^{-1}). Conformational analysis over each torsion of PDO yields 729 structures, from which Chen *et al*. reported that only 109 structures are feasible conformers at the MP2/6-311++G(3df,3pd) level of theory.[49] These structures were further optimized at the M06-2X/cc-pVTZ level of theory in this work, reducing the number of conformations to 99. **Table 2E** presents the most stable conformation for PDO, stabilized by internal hydrogen bonds. Such intramolecular interactions have also been found in other diols like 1,3-propanediol[50] and 1,6-hexanediol[49].

The conformers of D1 were sought based on the results for HTHP. D1 consists of two stereoisomers: *R,S* and *R,R*. Both were explored and the lowest energy conformer was found to adopt the *R,R* configuration (**Table 2F**). The first higher energy conformer of D1 was observed with a 27.1 kJ mol^{-1} free energy higher than its global minimum, which does not contribute significantly in the overall computation of the thermodynamic properties of D1 at 298.15 K. Given that the boat conformations of HTHP did not play an important role in the contribution to the overall partition function, the conformations of D1 in which the rings adopt the boat configuration were assumed to not be favored and were therefore not included in this analysis.

A systematic search for conformers of large molecules like D2 with quantum-mechanical methods would result in 3^7 potential configurations, which is prohibitive.[51] Yalamanchi *et al.* overcame this challenge for other molecules by only considering the conformers whose potential energies ($\Delta\epsilon$) lie within 9.6 kJ mol^{-1} of the global minimum conformer.[52] In order to improve the chances of finding most of the minimum energy conformations of D2, the cut off in this work was expanded to $\Delta\epsilon$ = 23 kJ mol^{-1}. **Figure S2** displays the $\Delta\epsilon$ of the selected conformers of D2, PDO, 5-HP, HTHP, and D1 computed with the MMFF94 force field, along with their free energies (ΔG) at the M06-2X/cc-pVTZ level of theory. A linear trend is observed to exist between the $\Delta\epsilon$ and ΔG values, enabling the use of $\Delta\epsilon$ values as a descriptor to predict a set of meaningful conformers for D2. From the conformational search results for HTHP, 5-HP, and PDO herein, another observation was made – conformers with $\Delta G > 8.4$ kJ mol^{-1} above

the global minimum contribute insignificantly to their free energy of formation, ΔG_f^0 (**Figure S3).** Unlike linear molecules like 5-HP or PDO, as shown in **Figure S2**, D2 only has a few conformations that lie within the first 8.4 kJ mol^{-1}. **Table 2G** displays the minimum energy conformer of D2 optimized thorugh *ab initio* calculations, and is observed to exhibit a shape in which the chain forms a coil that reduces its potential energy.

Table 2. Skeletal structures and global minimum potential energy conformers calculated at the M06-2X/cc-pVTZ level of theory for: **A)** HTHP, **B)** 5-HP, **C)** DHP, **D)** DVL, **E)** PDO, **F)** D1, and **G)** D2.

Compound	**Skeletal structure**	**Lowest energy conformer**
A) 2-Hydroxy tetrahydropyran (HTHP)	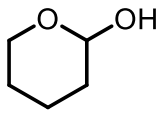	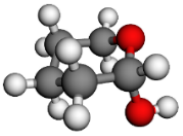
B) 5-Hydroxypentanal (5-HP)	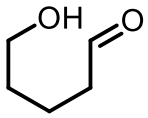	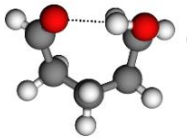
C) 3,4-Dihydropyran (DHP)	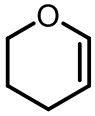	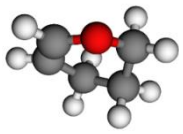
D) δ-Valerolactone (DVL)	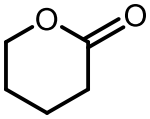	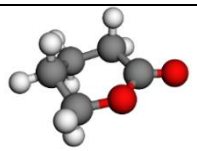
E) 1,5-Pentanediol (PDO)	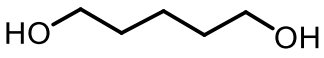	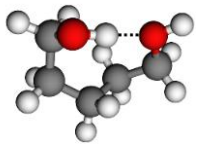
F) 2,2'-Oxybis(tetrahydropyran) (Dimer 1; D1)	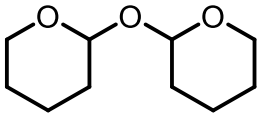	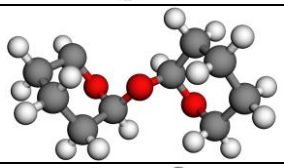
G) 5-(Tetrahydropyran-2-yloxy)pentanal (Dimer 2; D2)	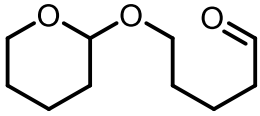	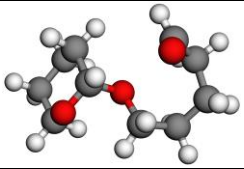

Table 3 lists the DFT-calculated standard enthalpy of formation (ΔH_f°), standard Gibbs free energy of formation (ΔG_f°), and constants *'a'* and *'b'* for calculation of the heat capacity (C_p). For comparison, thermochemistry data for DHP, PDO and 5-HP has been contrasted in **Figure S4** with data extracted from Aspen, as a way of validating the calculations in this work for molecules whose thermodynamic properties are unpublished. There is excellent agreement between the DFT-computed

properties of DHP, 5-HP, and PDO with the experimental data. Interestingly, the DFT-calculated values for DVL are in agreement with the experimentally reported NIST data but do not match the values predicted in Aspen for both ΔH_f° and ΔG_f°.[53] This is due to a discrepancy of -40.6 kJ mol^{-1} between the NIST data and the Aspen database, which is also nearly the same difference between the DFT-calculated results and the Aspen database. We conclude that the thermodynamic properties of DVL calculated herein from DFT (and verified experimentally by NIST) are more accurate than the Aspen database.

Table 3. DFT-calculated standard enthalpy of formation (ΔH_f°), standard Gibbs free energy of formation (ΔG_f°), and constants *a* and *b* to calculate heat capacities (C_p) for each compound in the reaction network.

Compound	ΔH_f° (kJ mol^{-1})	ΔG_f° (kJ mol^{-1})	*a* (J mol^{-1} K^{-1})	*b* (J mol^{-1} K^{-2})
2-HTHP	-412.33	-238.66	18.04	0.34
5-HP	-381.33	-240.20	36.89	0.32
DHP	-113.56	-1.09	12.05	0.28
DVL	-382.33	-249.07	21.40	0.30
1,5-PDO	-449.53	-266.73	36.79	0.35
D1	-603.88	-258.66	20.98	0.65
D2	-580.74	-259.32	44.13	0.62

Figure 5 displays the DFT-calculated thermochemistry (ΔH_{rxn} and ΔG_{rxn}) from 50–300 °C using **Equations (12)** and **(13)**, and the values listed in **Table 3**. The corresponding DFT-calculated equilibrium rate constants (K_{eq}) are shown in **Figure S5**, along with the experimentally determined K_{eq} listed in **Table 1**. The values are observed to be in good agreement for the temperature range studied, verifying the DFT calculations in this work. The unimolecular reactions of HTHP are endothermic in this temperature range (**Figure 5A**), with HTHP dehydration to DHP being the most endothermic (ΔH_{rxn} ~ 50 kJ mol^{-1}), followed by ring-opening of HTHP to 5-HP (ΔH_{rxn} ~ 32 kJ mol^{-1}) and HTHP dehydrogenation to DVL (ΔH_{rxn} ~ 29 kJ mol^{-1}). All bimolecular reactions involving HTHP, DHP and/or H_2 are observed to be exothermic, including HTHP dimerization to D2 (ΔH_{rxn} ~ -26 kJ mol^{-1}), HTHP hydrogenation to PDO (ΔH_{rxn} ~ -40 kJ mol^{-1}), and acetalization of DHP with HTHP to D2 (ΔH_{rxn} ~ -52 kJ mol^{-1}) and D1 (ΔH_{rxn} ~ -78 kJ mol^{-1}). HTHP dimerization to D2 is slightly endothermic (ΔH_{rxn} ~ 1kJ mol^{-1}) at T<125°C but becomes exothermic at higher temperatures (ΔH_{rxn} = -6 kJ mol^{-1} at 300°C). From the plot of ΔG_{rxn} over 50–300 °C (**Figure 5B**), two trends are observed: 1) HTHP dehydrogenation to DVL, ring-opening to 5-HP, dehydration to DHP, and dimerization to D2, are all increasingly exergonic with increasing temperatures; 2) HTHP hydrogenation to PDO, HTHP dimerization to D1, and DHP acetalization with HTHP to D1 and D2 follow the opposite trend – becoming more endergonic at higher temperatures. At T>130°C, HTHP dehydrogenation to DVL is the most exergonic reaction, with ΔG_{rxn} decreasing from -24 kJ mol^{-1} at 130°C to -46 kJ mol^{-1} at 300°C. HTHP hydrogenation to PDO becomes the most exergonic reaction at T<130°C but is limited by the availability of H_2 when the reaction is carried out in an inert atmosphere. At 82°C, HTHP hydration to DHP is at equilibrium (ΔG_{rxn} = 0 kJ mol^{-1}), but becomes spontaneous (ΔG_{rxn} = -32 kJ mol^{-1}) by 300°C. Within the 100 – 250°C temperature range, 3 other reactions also attain equilibrium at certain temperatures: DHP and HTHP acetalization to D1 (120°C), DHP and HTHP acetalization to D2 (195°C), and HTHP dimerization to D1 (230°C). Although the complexity of the experimentally-observed reaction network can be understood by all the reactions being exergonic at 85–120°C (**Figure 5B**), the dominance of DVL formation in the temperature range of T>130°C rationalizes its successful synthesis from HTHP in our experiments.

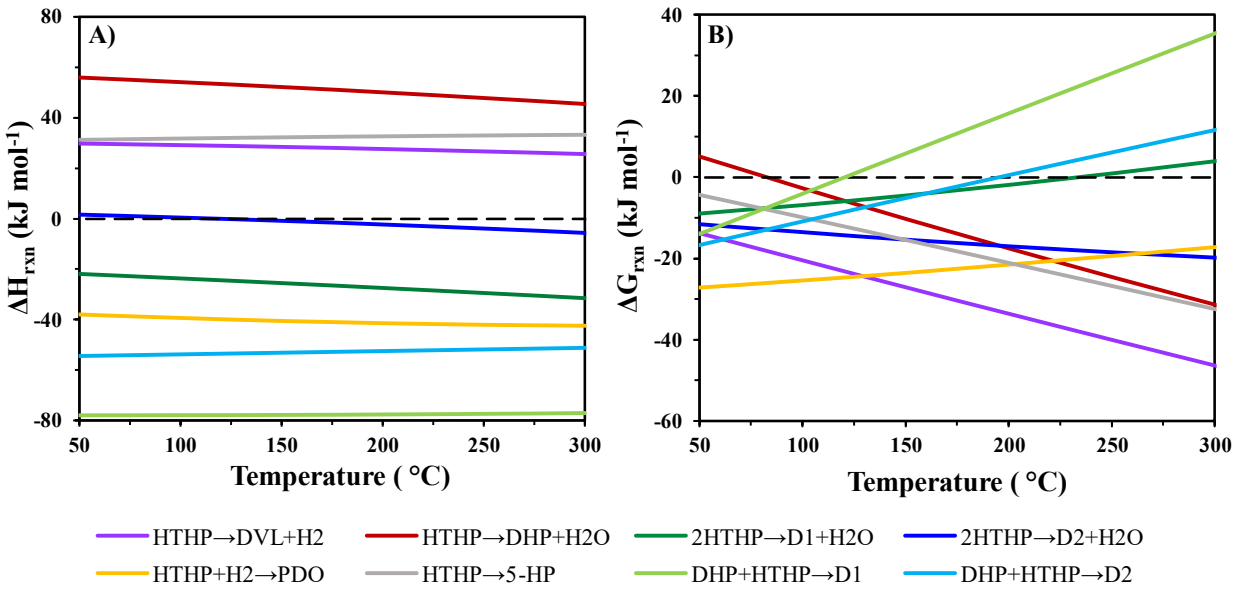

Figure 5. DFT-calculated thermochemistry for **A)** ΔH_{rxn} and **B)** ΔG_{rxn} at the M06-2X/cc-pVTZ level of theory for the thermocatalytic reactions between HTHP, DHP, 5-HP, DVL, D1, D2, and PDO. Dashed lines at 0 kJ mol^{-1} are visual aids.

4) Effect of temperature on HTHP dehydrogenation over Cu/SiO$_2$

In the next few sections, HTHP dehydrogenation over Cu/SiO$_2$ was studied using a packed bed reactor to acquire kinetic data since this catalyst has the highest rates and selectivities to DVL. The effect of temperature on the turnover frequency (TOF) and selectivity of each product over Cu/SiO$_2$ is shown in **Figure 6**. TOF was calculated using the Cu site density of Cu/SiO$_2$, as listed in **Table S2.** Reactions were carried out for 24 hours to obtain steady-state samples, and a fresh bed of Cu/SiO$_2$ was used for each temperature to rule out catalyst deactivation. Minimal HTHP conversion was observed at T<100°C, and the carbon balance was ~98% for all experiments carried out at 125–250°C. The major product observed from HTHP over Cu/SiO$_2$ at all temperatures was DVL. At 125°C, HTHP conversion was only 7.5% with DVL produced at a TOF of 0.07 min^{-1}, corresponding to a selectivity of 61%. As the temperature was raised to 150°C, HTHP conversion increased to 19% while DVL formation jumped to 0.25 min^{-1}, reaching a peak DVL selectivity of 75.5%. Between 125–150°C, the selectivity to DHP and D1 remained nearly constant at 6.1 and 5.5%, respectively, while the selectivity to D2 dropped from 26.3 to 13.6%. With further increase in temperature to 250°C, HTHP conversion reached 77% but the selectivity to DVL dropped to 39% as the TOF of DHP production increased 10× from 0.02 min^{-1} to 0.22 min^{-1}, and D2 increased 6× from 0.05 min^{-1} to 0.3 min^{-1}. The apparent activation energies (E_a) and pre-exponential factors (A) for DVL, DHP, D1, and D2 formation were determined from data collected at 125–175°C within the kinetic regime (HTHP conversion < 20%). As shown in **Table 4**, the E_a for each product decreases in the following order: DVL (36.9 ± 1.3 kJ mol^{-1}) < D1 (50.7 ± 0.5 kJ mol^{-1}) ≈ D2 (51.5 ± 0.7 kJ mol^{-1}) ≈ DHP (53.9 ± 1.1 kJ mol^{-1}). The E_a for HTHP hydration to DHP is observed to be 25 kJ mol^{-1} lower than the E_a for DHP hydration to HTHP (78.8 ± 1.5 kJ mol^{-1}),[25] albeit the latter was determined at 25 – 62.5°C using 20 wt% DHP in water. The similarity in apparent activation energies for D1, D2, and DHP formation further corroborates the formation of a common carbocation intermediate from HTHP, as shown in **Scheme 3**.

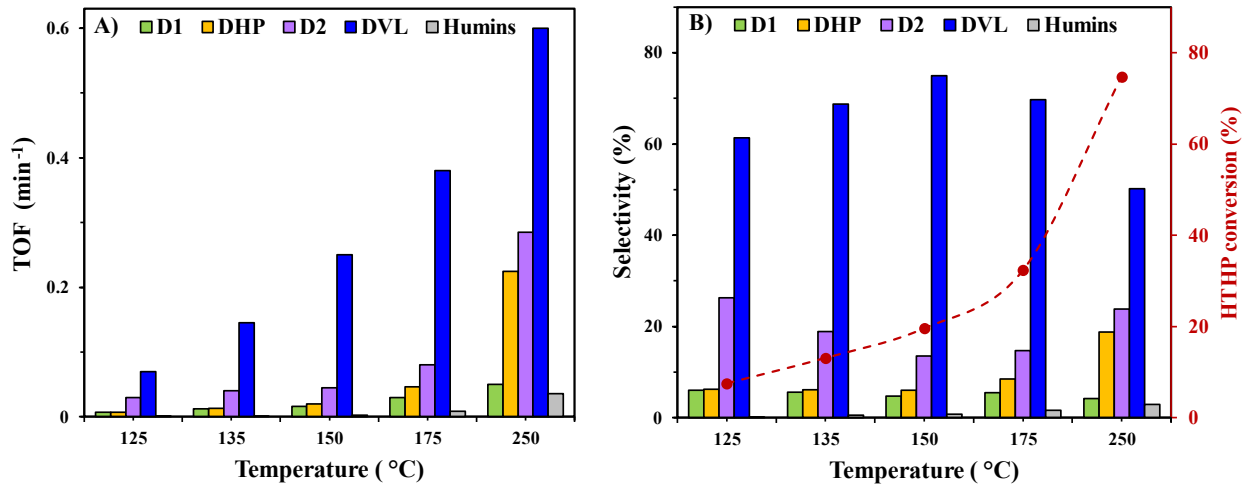

Figure 6. Effect of reaction temperature on: **A)** turnover frequency (TOF), and **B)** selectivity and HTHP conversion. Reaction conditions: 125–250°C, 1 min^{-1} WHSV, 0.1 mL/min 10 wt% HTHP in THP, 0.1 g Cu/SiO_2, 50 mL/min Ar, 200 psi, 24 h at each contact time.

5) Effect of contact time on HTHP dehydrogenation over Cu/SiO_2

The effect of contact time on TOF and selectivities was studied by varying the contact time from 0.5 to 31.5 min at a fixed reaction temperature of 150°C (**Figure 7**). At 0.5 min, DVL was produced at a TOF of 0.25 min^{-1}. As the contact time was increased from 1.1 to 14.3 min, the TOF of DVL production quadrupled from 0.25 to 1 min^{-1} while the selectivity to DVL increased from 68 to 75%. HTHP conversion increased from 9 to 86% as the contact time was increased from 0.5 – 31.5 min. With further increases in contact time to 31.5 min, the TOF of DVL production dropped to 0.8 min^{-1} and DVL selectivity reached a minimum of 58%. The temperature and contact time experiments herein reveal that intermediate contact times of ~14.3 min at 150 °C are needed to maximize selectivity to DVL.

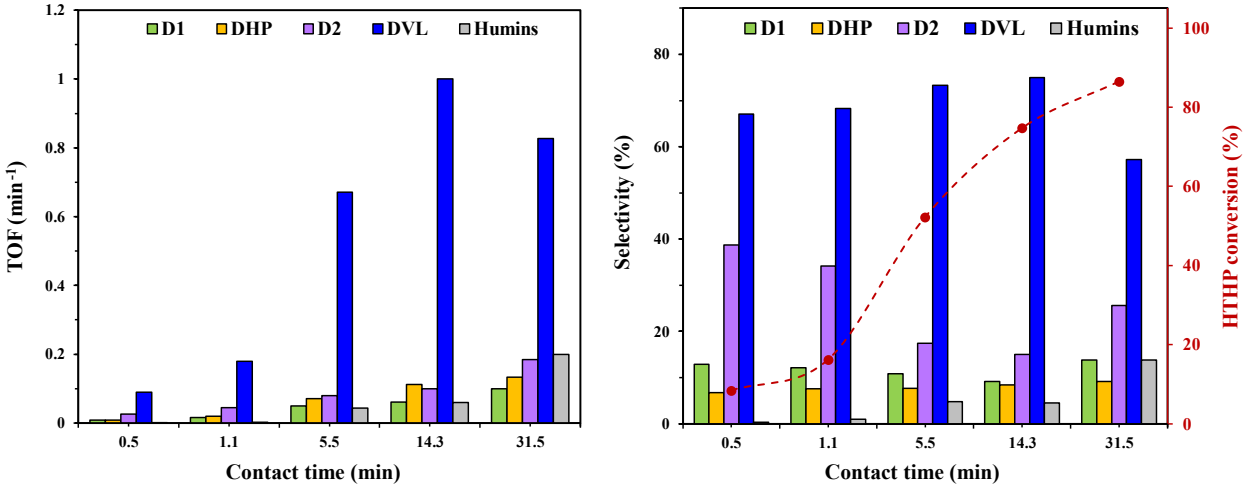

Figure 7. Effect of contact time on: **A)** turnover frequency (TOF), and **B)** selectivity and HTHP conversion. Reaction conditions: 150 °C, 0.86–0.01 min^{-1} WHSV, 50 mL/min Ar, 200 psi, 24 h at each WHSV, Cu/SiO_2.

6) Determining reaction orders from partial pressure experiments

Reaction orders with respect to HTHP were determined by varying the HTHP partial pressure (P_{HTHP}) from 1.7 to 4.7 psi, while keeping the temperature, contact time, and total pressure constant at 150°C, 1 min, and 200 psi, respectively. **Figure 8** shows the log-log plot of TOF versus P_{HTHP} along with

the reaction orders (*n*) determined from the slope of each curve. As P_{HTHP} was increased from 1.7 to 4.7 psi, the TOF of DVL formation tripled from 0.14 to 0.42 min^{-1}, while DHP quadrupled from 0.01 to 0.04 min^{-1}. As seen from the slope of the DVL and DHP curves, HTHP dehydrogenation to DVL and HTHP dehydration to DHP are both nearly 1st order in HTHP partial pressure. On the other hand, D1 and D2 rates increased 7× from 0.01 to 0.07 min^{-1}, and 0.04 to 0.28 min^{-1}, respectively, when P_{HTHP} was increased from 1.7 to 4.7 psi. Correspondingly, HTHP acetalization to D1 and D2 are both observed to be 2nd order with respect to P_{HTHP}.

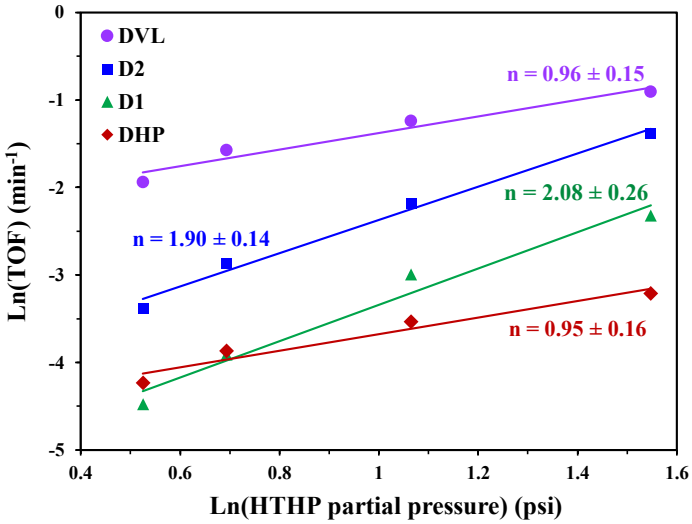

Figure 8. Log-log plots of product turnover frequencies (TOF) versus HTHP partial pressure (P_{HTHP}) for determination of reaction orders (*n*) from the slope of each curve. Reaction conditions: 150 °C, 1 min contact time, 0.1 mL/min HTHP in THP, 0.1 g Cu/SiO_2, 200 psi, 24 h at each partial pressure. Solid lines are visual aids.

8) Development of a reaction kinetics model

Based on the experiments carried out at varying reaction temperatures, contact times, and HTHP partial pressures, a kinetic model was developed. The 8 reactions used in the model are shown in **Scheme 4**.

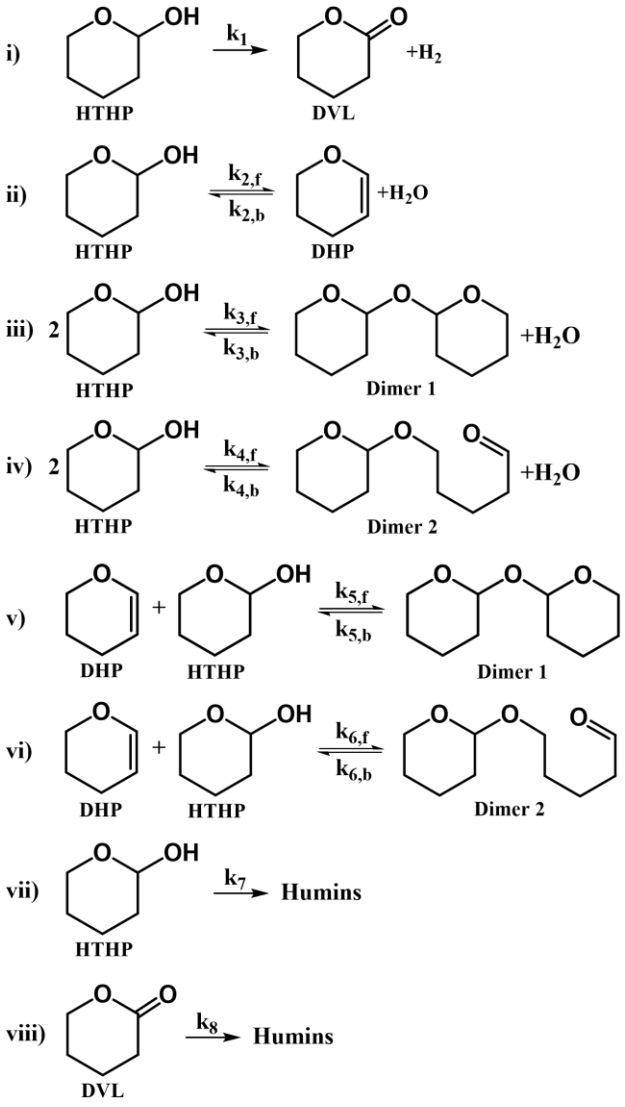

Scheme 4. Reaction network for the dehydrogenation of HTHP to DVL (i), thermal equilibrium between HTHP, DHP, D1, and D2 (ii – vi), and formation of degradation products (vii & viii).

The corresponding ordinary differential equations (ODEs) used in the kinetic model are listed in **Eqn 14–19**.

$$\frac{d[DVL]}{d\tau} = k_1[HTHP] - k_8[DVL] \quad \textbf{(14)}$$

$$\frac{d[HTHP]}{d\tau} = -k_1[HTHP] - k_{2,f}[HTHP] + k_{2,b}[DHP][H_2O] - 2k_{3,f}[HTHP]^2 + 2k_{3,b}[D1][H_2O] - 2k_{4,f}[HTHP]^2 + 2k_{4,b}[D2][H_2O] - k_{5,f}[HTHP][DHP] + k_{5,b}[D1] - k_{6,f}[HTHP][DHP] + k_{6,b}[D2] - k_7[HTHP] \quad \textbf{(15)}$$

$$\frac{d[DHP]}{d\tau} = k_{2,f}[HTHP] - k_{2,b}[DHP][H_2O] - k_{5,f}[HTHP][DHP] + k_{5,b}[D1] - k_{6,f}[HTHP][DHP] + k_{6,b}[D2] \quad \textbf{(16)}$$

$$\frac{d[D1]}{d\tau} = k_{3,f}[HTHP]^2 - k_{3,b}[D1][H_2O] + k_{5,f}[HTHP][DHP] - k_{5,b}[D1] \quad \textbf{(17)}$$

$$\frac{d[D2]}{d\tau} = k_{4,f}[HTHP]^2 - k_{4,b}[D2][H_2O] + k_{6,f}[HTHP][DHP] - k_{6,b}[D2] \quad \textbf{(18)}$$

$$\frac{d[Humins]}{d\tau} = k_7[HTHP] + k_8[DVL] \quad \textbf{(19)}$$

The forward rate constants as a function of temperature, $k_f\ (T)$, were determined using the Arrhenius relationship in **Eq 20**, wherein k_f^{ref} is the experimentally determined forward rate constant at T_{ref} = 423.15 K with apparent activation energy E_a (as listed in **Table 4**). The backward rate constants, $k_b\ (T)$, were determined from **Eq 21**, wherein $K_{eq}\ (T)$ is the DFT-calculated equilibrium rate constant from **Equation (13)**.

$$k_f(T) = k_f^{ref} \exp\left[-\frac{E_a}{R}\left(\frac{1}{T} - \frac{1}{T_{ref}}\right)\right] \quad \textbf{(20)}$$

$$k_b(T) = \frac{k_f(T)}{K_{eq}(T)} \quad \textbf{(21)}$$

Table 4. Model-predicted forward rate constants (k_f) and apparent activation energies (E_a), with associated 95% confidence intervals, for the thermocatalytic reactions between HTHP, DVL, DHP, D1, D2, and humins in a packed bed reactor over Cu/SiO_2 under Ar atmosphere.

Reaction	Forward rate constants, k_f^{ref}, at T_{ref} = 150°C	Apparent activation energies, E_a (kJ mol^{-1})
R1: HTHP → DVL + H_2	0.11 ± 0.02 min^{-1}	36.9 ± 1.3
R2: HTHP → DHP + H_2O	0.014 ± 0.002 min^{-1}	48.5 ± 0.5
R3: 2HTHP → D1 + H_2O	0.005 ± 0.001 mM^{-1} min^{-1}	50.2 ± 0.7
R4: 2HTHP → D2 + H_2O	0.015 ± 0.006 mM^{-1} min^{-1}	51.7 ± 1.1
R5: HTHP + DHP → D1	0.002 ± 0.0008 mM^{-1} min^{-1}	63.5 ± 1.3
R6: HTHP + DHP → D2	0.003 ± 0.0005 mM^{-1} min^{-1}	68.9 ± 1.5
R7: HTHP → Humins	0.004 ± 0.001 min^{-1}	40.2 ± 0.9
R8: DVL → Humins	0.02 ± 0.003 1 min^{-1}	30.5 ± 0.4

The resulting model-predicted selectivity to DVL as a function of temperature (145 – 155°C) and contact time (0 – 20 minutes) is shown as a heatmap in **Figure 9**. At low temperatures, the rate of DVL production is too low, leading to lower selectivities. At long contact times, humin production increases, also leading to lower DVL selectivities. DVL selectivity can be maximized at 78% by carrying out HTHP dehydrogenation at a temperature of 145°C and contact time of 12.8 minutes.

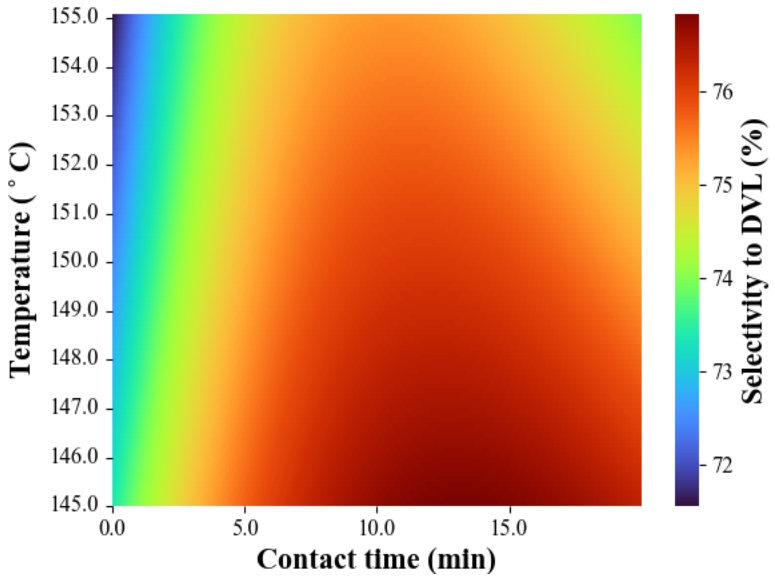

Figure 9. Heatmap of model-predicted selectivity to DVL from dehydrogenation of HTHP over Cu/SiO_2 as a function of temperature and contact time. DVL selectivity is maximized at 78% at 145°C and 12.8 minutes.

7) Catalyst stability as a function of time on stream (TOS)

HTHP dehydrogenation over Cu/SiO_2 at the reaction conditions that maximized DVL selectivity (~150°C and 13 minutes of contact time) was carried out in a flow reactor for 72 h time on stream (TOS) to determine catalyst deactivation rates (**Figure 10**). The TOF of DVL formation increased slightly from 49 to 52 min^{-1} in the first 8 h then remained constant at ~52 min^{-1} until 32 h, indicating that steady state was achieved. The corresponding selectivity to DVL reached a maximum of 84% at 12 hours, in agreement with the model-predicted DVL selectivity at these conditions. By 72 h, the TOF of DVL dropped to 42 min^{-1} and the selectivity to DVL decreased to 74%. Similarly, HTHP conversion was ~90% for 48 h but dropped to 81% by 72 h, indicating loss of catalyst activity. The TOF of D2, DHP, and D1 formation was always <5 min^{-1}. But the selectivity to D1 and D2 increase to 8% and 19%, respectively, around 60 h. The loss in HTHP conversion and DVL rates, accompanied by the increase in rates of D1 and D2, indicate that the formation of C_{10+} species on the catalyst surface is likely contributing to catalyst deactivation via coking. Thermogravimetric analysis (TGA) of the fresh and spent Cu/SiO_2 confirmed that coking contributed to 14% of the mass of the spent catalyst (**Figure S5**). A small loss in BET surface area of the Cu/SiO_2 catalyst was also observed (**Table S2)**, indicating that pore blocking is minimaly contributing to the loss of catalyst activity over time. ICP-OES results indicate little to no metal leaching. We also measured the Cu site density and dispersion of the Cu/SiO_2 catalysts before and after reaction (**Table S2**) and observed minimal changes in both properties, indicating that sintering or loss of Cu dispersion is not contributing to catalyst deactivation in this work. After 72 h, the catalyst was regenerated by calcining in 2% O_2/Ar at 400°C, followed by re-reduction in H_2 flow at 350°C. The reaction was resumed and carried out for another 48 h. At 80 h, much of the catalyst activity and selectivity to DVL was recovered and comparable to that of the fresh catalyst. By 120 h, the TOF and selectivity to DVL had dropped to 42 min^{-1} and 82%, respectively. Hence, we have demonstrated that DVL can be produced at >75% selectivity for over 72 h with minor losses in catalyst activity from coking and pore blocking.

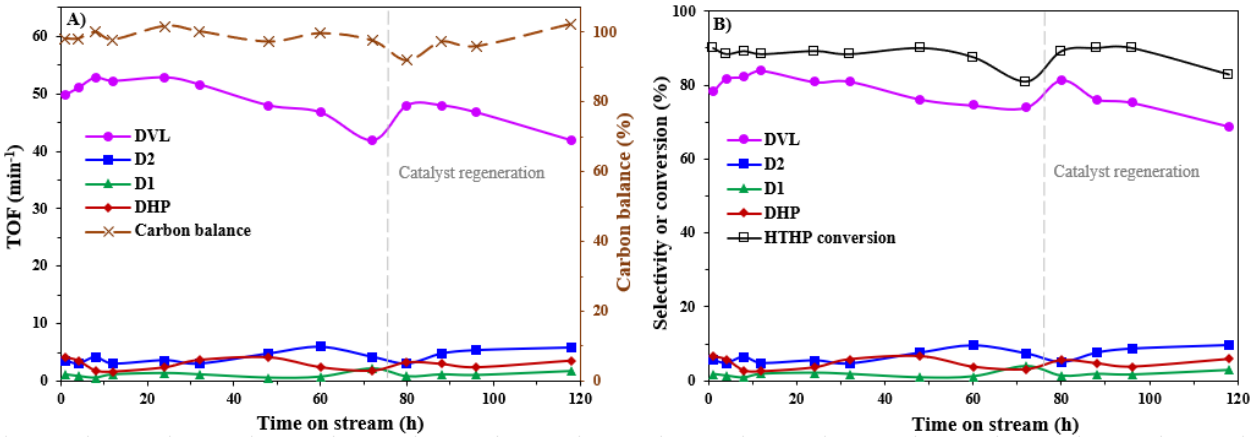

Figure 10. Effect of time on stream (TOS) on: **A)** turnover frequency (TOF) and carbon balance, and **B)** product selectivity and HTHP conversion. Reaction conditions: 150°C, 13 min contact time, 0.1 g 20wt% Cu/SiO_2, 50 mL/min Ar, 200 psi. After 72 h, catalyst is regenerated via calcination and re-reduction, then reaction is carried out till 120 h. Lines through data points are visual aids.

Conclusions

Biomass-derived 2-hydroxytetrahydropyran (HTHP) is an emerging platform chemical for the renewable production of five-carbon (C5) compounds, which are otherwise very hazardous and expensive to produce from petroleum. Herein, a novel catalytic route to δ-valerolactone (DVL) has been reported at 84% selectivity from dehydrogenation of HTHP in a packed bed reactor over Cu/SiO_2 at 150°C and 13 minutes of contact time. Cu/SiO_2 has the highest rate and selectivity to DVL production out of all the catalysts screened. We have also discovered that HTHP exists in thermal equilibrium with 3 other compounds: 3,4-dihydropyran (DHP), 2,2'-oxybis(tetrahydropyran) (Dimer 1; D1), and 5-(tetrahydropyran-2-yloxy)pentanal (Dimer 2; D2), due to the formation of a common carbocation intermediate. Since the thermochemical data for HTHP, D1, and D2 cannot be found in existing databases, DFT calculations at the M06-2X/cc-pVTZ level of theory were carried out to reveal that HTHP dehydrogenation to DVL is the most exergonic reaction ($\Delta G_{rxn}<0$) at T>125°C. Using kinetic studies, we also determined that DVL formation has an apparent activation energy (E_a) of 36.9 ± 1.3 kJ mol^{-1} and is first-order with respect to HTHP partial pressure (P_{HTHP}). Lastly, we developed a kinetic model consisting of eight ordinary differential equations (ODEs) to predict DVL selectivity as a function of both reaction temperature and contact time, and experimentally verified the model-predicted values with a 72-hour reaction.

Declaration of Competing Interest

The authors declare the following financial interests/personal relationships which may be considered as potential competing interests. George Willis Huber reports financial support was provided by US Department of Energy (DOE). RGD, DJM, and GWH have a patent, titled "Catalytic Synthesis of Delta-Valerolactone (DVL) from Furfural-Derived 2-Hydroxytetrahydropyran (HTHP)." Submitted to Wisconsin Alumni Research Foundation (WARF). RGD, DJM and GWH have a financial interest in Pyran, Inc. which is commercializing the technology to produce biomass-based C5 chemicals from furfural. All other authors declare that they have no known competing financial interests or personal relationships that could have appeared to influence the work reported in this paper.

Acknowledgements

RGD was supported by the University of Wisconsin-Madison's Discovery to Product (D2P) with funding from the State of Wisconsin. This work was funded by the U.S. Department of Energy, Office of Energy

Efficiency and Renewable Energy, Bioenergy Technologies Office under contract no. DE-EE0009305. The views and opinions of the authors expressed herein do not necessarily state or reflect those of the U.S. Government or any agency thereof or of any commercial entity.

Author contributions

RGD carried out all experiments and kinetic modeling. JEC and ZJ performed DFT calculations. RGD and JEC drafted the manuscript. DJM, MM and GWH oversaw the project, assisted with funding acquisition, supervised experimental and computational design, and reviewed the manuscript. All authors have read and approved the final manuscript.

Intellectual property

A patent application for this work, PCT/US2023/079965, was filed through the Wisconsin Alumni Research Foundation (WARF) on November 16, 2023.

References

1. Medical Plastics Market Size, Share & COVID-19 Impact Analysis, By Application, and Regional Forecast, 2020-2027. Fortune Business Insights. https://www.fortunebusinessinsights.com/medical-plastics-market-102136 (accessed 2023-10-02).
2. Li, X.-L.; Clarke, R. W.; An, H.-Y.; Gowda, R. R.; Jiang, J.-Y.; Xu, T.-Q.; Chen, E. Y.-X., Dual Recycling of Depolymerization Catalyst and Biodegradable Polyester that Markedly Outperforms Polyolefins. *Angewandte Chemie International Edition* **2023**, e202303791.
3. Da Silva, D.; Kaduri, M.; Poley, M.; Adir, O.; Krinsky, N.; Shainsky-Roitman, J.; Schroeder, A., Biocompatibility, biodegradation and excretion of polylactic acid (PLA) in medical implants and theranostic systems. *Chemical Engineering Journal* **2018,** *340*, 9-14.
4. Hu, Z.; Chen, Y.; Huang, H.; Liu, L.; Chen, Y., Well-Defined Poly(α-amino-δ-valerolactone) via Living Ring-Opening Polymerization. *Macromolecules* **2018,** *51* (7), 2526-2532.
5. Badwelan, M.; Alkindi, M.; Alghamdi, O.; Saeed, W. S.; Al-Odayni, A.-B.; Alrahlah, A.; Aouak, T., Poly (δ-valerolactone)/Poly (ethylene-co-vinylalcohol)/β-Tricalcium Phosphate Composite as Scaffolds: Preparation, Properties, and In Vitro Amoxicillin Release. *Polymers* **2020,** *13* (1), 46.
6. Zhang, D.; Dashtimoghadam, E.; Fahimipour, F.; Hu, X.; Li, Q.; Bersenev, E. A.; Ivanov, D. A.; Vatankhah-Varnoosfaderani, M.; Sheiko, S. S., Tissue-Adaptive Materials with Independently Regulated Modulus and Transition Temperature. *Advanced Materials* **2020,** *32* (50), 2005314.
7. Le Devedec, F.; Boucher, H.; Dubins, D.; Allen, C., Factors Controlling Drug Release in Cross-linked Poly(valerolactone) Based Matrices. *Molecular Pharmaceutics* **2018,** *15* (4), 1565-1577.
8. Li, X.-L.; Clarke, R. W.; Jiang, J.-Y.; Xu, T.-Q.; Chen, E. Y.-X., A circular polyester platform based on simple gem-disubstituted valerolactones. *Nature Chemistry* **2023,** *15* (2), 278-285.
9. Alonso, D. M.; Wettstein, S. G.; Dumesic, J. A., Gamma-valerolactone, a sustainable platform molecule derived from lignocellulosic biomass. *Green Chemistry* **2013,** *15* (3), 584-595.
10. Kojčinović, A.; Kovačič, Ž.; Huš, M.; Likozar, B.; Grilc, M., Furfural hydrogenation, hydrodeoxygenation and etherification over MoO2 and MoO3: A combined experimental and theoretical study. *Applied Surface Science* **2021,** *543*, 148836.
11. Dastidar, R. G.; Kim, M. S.; Zhou, P.; Luo, Z.; Shi, C.; Barnett, K. J.; McClelland, D. J.; Chen, E. Y.-X.; Van Lehn, R. C.; Huber, G. W., Catalytic production of tetrahydropyran (THP): a biomass-derived, economically competitive solvent with demonstrated use in plastic dissolution. *Green Chemistry* **2022,** *24* (23), 9101-9113.
12. Mercker, H. J.; Pape, F.-F.; Simon, J.; Henne, A.; Hesse, M.; Kohler, U.; Dostalek, R.; Erdbrugger, C. F.; Kratz, D. Dehydrogenation of 1, 4-butanediol to γ-butyrolactone. US5955620A, 1999.
13. Bohnet, M., *Ullmann's encyclopedia of industrial chemistry*. 6th, completely rev. ed ed.; Wiley-VCH Weinheim: Weinheim, 2003.
14. Ma, Q.; Xue, Y.; Guo, J.; Peng, X., The Baeyer–Villiger Oxidation of Cycloketones Using Hydrogen Peroxide as an Oxidant. *Catalysts* **2022,** *13* (1), 21.

15. Cyclohexanone Price Trend and Forecast. ChemAnalyst. https://www.chemanalyst.com/Pricing-data/cyclohexanone (accessed 2023-09-25).
16. Zhou, W.-J.; Wischert, R.; Xue, K.; Zheng, Y.-T.; Albela, B.; Bonneviot, L.; Clacens, J.-M.; De Campo, F.; Pera-Titus, M.; Wu, P., Highly Selective Liquid-Phase Oxidation of Cyclohexane to KA Oil over Ti-MWW Catalyst: Evidence of Formation of Oxyl Radicals. *ACS Catalysis* **2014,** *4* (1), 53-62.
17. Van Asselt, W.; Van Krevelen, D., Preparation of adipic acid by oxidation of cyclohexanol and cyclohexanone with nitric acid: Part I. Reaction mechanism. *Recueil des Travaux Chimiques des Pays-Bas* **1963,** *82* (1), 51-67.
18. Renz, M., Ketonization of carboxylic acids by decarboxylation: mechanism and scope. *European journal of organic chemistry* **2005,** *2005* (6), 979-988.
19. Wang, H.; Ding, G.; Li, X.; She, H.; Zhu, Y.; Li, Y., Sustainable production of γ-valerolactone and δ-valerolactone through the coupling of hydrogenation and dehydrogenation. *Sustainable Energy & Fuels* **2021,** *5* (4), 930-934.
20. Pinkos, R.; Bauduin, C.; Paul, A.; Fritz, G.; Wagner, H., Process for preparing delta-valerolactone in the gas phase. U.S. Patents: 2013.
21. Paris, G.; Berlinguet, L.; Gaudry, R.; English Jr., J.; Dayan, J. E., Glutaric Acid and Glutarimide. In *Organic Syntheses*, 2003; pp 47-47.
22. Narisetty, V.; Cox, R.; Bommareddy, R.; Agrawal, D.; Ahmad, E.; Pant, K. K.; Chandel, A. K.; Bhatia, S. K.; Kumar, D.; Binod, P., Valorisation of xylose to renewable fuels and chemicals, an essential step in augmenting the commercial viability of lignocellulosic biorefineries. *Sustainable Energy & Fuels* **2022,** *6* (1), 29-65.
23. Furfural Market by Raw Material (Sugarcane Bagasse, Corncob, Rice Husk and Others), Application (Derivatives (Furfural Alcohol and Other Derivatives), solvent) and Region (Asia-Pacific, Americas, Europe,Middle East and Africa) - Global Forecast to 2024. https://www.marketsandmarkets.com/Market-Reports/furfural-market-101056456.html.
24. Li, L.; Barnett, K. J.; McClelland, D. J.; Zhao, D.; Liu, G.; Huber, G. W., Gas-phase dehydration of tetrahydrofurfuryl alcohol to dihydropyran over γ-Al2O3. *Applied Catalysis B: Environmental* **2019,** *245*, 62-70.
25. Barnett, K. J.; McClelland, D. J.; Huber, G. W., Autocatalytic hydration of Dihydropyran to 1, 5-Pentanediol precursors via in situ formation of liquid-and solid-phase acids. *ACS Sustainable Chemistry & Engineering* **2017,** *5* (11), 10223-10230.
26. Brentzel, Z. J.; Barnett, K. J.; Huang, K.; Maravelias, C. T.; Dumesic, J. A.; Huber, G. W., Chemicals from biomass: Combining ring-opening tautomerization and hydrogenation reactions to produce 1, 5-pentanediol from furfural. *ChemSusChem* **2017,** *10* (7), 1351-1355.
27. Li, X.; Tian, J.; Liu, H.; Hu, X.; Zhang, J.; Xia, C.; Chen, J.; Liu, H.; Huang, Z., Efficient Synthesis of 5-Amino-1-pentanol from Biomass-Derived Dihydropyran over Hydrotalcite-Based Ni–Mg3AlOx Catalysts. *ACS Sustainable Chemistry & Engineering* **2020,** *8* (16), 6352-6362.
28. Pyran Expands 1,5 PDO Availability to Bring High-Performance, Bio-Based Diol to Market. https://pyranco.com/pyran-expands-15-pdo-availability-to-bring-high-performance-bio-based-diol-to-market/ (accessed 01/23/2024).
29. Huang, K.; Brentzel, Z. J.; Barnett, K. J.; Dumesic, J. A.; Huber, G. W.; Maravelias, C. T., Conversion of furfural to 1, 5-pentanediol: Process synthesis and analysis. *ACS Sustainable Chemistry & Engineering* **2017,** *5* (6), 4699-4706.
30. Chai, J.-D.; Head-Gordon, M., Long-range corrected hybrid density functionals with damped atom–atom dispersion corrections. *Physical Chemistry Chemical Physics* **2008,** *10* (44), 6615-6620.
31. Clark, T.; Chandrasekhar, J.; Spitznagel, G. W.; Schleyer, P. V. R., Efficient diffuse function-augmented basis sets for anion calculations. III. The 3-21+G basis set for first-row elements, Li–F. *Journal of Computational Chemistry* **1983,** *4* (3), 294-301.
32. Ditchfield, R.; Hehre, W. J.; Pople, J. A., Self-Consistent Molecular-Orbital Methods. IX. An Extended Gaussian-Type Basis for Molecular-Orbital Studies of Organic Molecules. *The Journal of Chemical Physics* **1971,** *54* (2), 724-728.

33. Pedretti, A.; Mazzolari, A.; Gervasoni, S.; Fumagalli, L.; Vistoli, G., The VEGA suite of programs: an versatile platform for cheminformatics and drug design projects. *Bioinformatics* **2020,** *37* (8), 1174-1175.
34. Hanwell, M. D.; Curtis, D. E.; Lonie, D. C.; Vandermeersch, T.; Zurek, E.; Hutchison, G. R., Avogadro: an advanced semantic chemical editor, visualization, and analysis platform. *Journal of Cheminformatics* **2012,** *4* (1), 17.
35. Hanwell, M. D.; Curtis, D. E.; Lonie, D. C.; Vandermeersch, T.; Zurek, E.; Hutchison, G. R. *Avogadro: an open-source molecular builder and visualization tool. Version 1.1.1*, 1.1.1; 2012.
36. Halgren, T. A., Merck molecular force field. I. Basis, form, scope, parameterization, and performance of MMFF94. *Journal of Computational Chemistry* **1996,** *17* (5-6), 490-519.
37. Zhao, Y.; Truhlar, D. G., The M06 suite of density functionals for main group thermochemistry, thermochemical kinetics, noncovalent interactions, excited states, and transition elements: two new functionals and systematic testing of four M06-class functionals and 12 other functionals. *Theoretical Chemistry Accounts* **2008,** *120* (1), 215-241.
38. Jr., T. H. D., Gaussian basis sets for use in correlated molecular calculations. I. The atoms boron through neon and hydrogen. *The Journal of Chemical Physics* **1989,** *90* (2), 1007-1023.
39. Frisch, M. J.; Trucks, G. W.; Schlegel, H. B.; Scuseria, G. E.; Robb, M. A.; Cheeseman, J. R.; Scalmani, G.; Barone, V.; Mennucci, B.; Petersson, G. A.; Nakatsuji, H.; Caricato, M.; Li, X.; Hratchian, H. P.; Izmaylov, A. F.; Bloino, J.; Zheng, G.; Sonnenberg, J. L.; Hada, M.; Ehara, M.; Toyota, K.; Fukuda, R.; Hasegawa, J.; Ishida, M.; Nakajima, T.; Honda, Y.; Kitao, O.; Nakai, H.; Vreven, T.; Montgomery Jr., J. A.; Peralta, J. E.; Ogliaro, F.; Bearpark, M. J.; Heyd, J. J.; Brothers, E. N.; Kudin, K. N.; Staroverov, V. N.; Keith, T. A.; Kobayashi, R.; Normand, J.; Raghavachari, K.; Rendell, A. P.; Burant, J. C.; Iyengar, S. S.; Tomasi, J.; Cossi, M.; Rega, N.; Millam, J. M.; Klene, M.; Knox, E.; Cross, J. B.; Bakken, V.; Adamo, C.; Jaramillo, J.; Gomperts, R.; Stratmann, R. E.; Yazyev, O.; Austin, A. J.; Cammi, R.; Pomelli, C.; Ochterski, J. W.; Martin, R. L.; Morokuma, K.; Zakrzewski, V. G.; Voth, G. A.; Salvador, P.; Dannenberg, J. J.; Dapprich, S.; Daniels, A. D.; Farkas, O.; Foresman, J. B.; Ortiz, J. V.; Cioslowski, J. *Gaussian 09 Rev. D.01*, Wallingford, CT, 2013.
40. NIST Computational Chemistry Comparison and Benchmark Database. 2022 ed.; Johnson III, R. D., Ed. NIST Standard Reference Database Number 101: doi:10.18434/T47C7Z, 2022.
41. Suárez, E.; Díaz, N.; Suárez, D., Entropy Calculations of Single Molecules by Combining the Rigid–Rotor and Harmonic-Oscillator Approximations with Conformational Entropy Estimations from Molecular Dynamics Simulations. *Journal of Chemical Theory and Computation* **2011,** *7* (8), 2638-2653.
42. Pracht, P.; Grimme, S., Calculation of absolute molecular entropies and heat capacities made simple. *Chemical Science* **2021,** *12* (19), 6551-6568.
43. Bautista, F. M.; Campelo, J. M.; García, A.; Luna, D.; Marinas, J. M.; Quirós, R. A.; Romero, A. A., Influence of acid–base properties of catalysts in the gas-phase dehydration–dehydrogenation of cyclohexanol on amorphous AlPO4 and several inorganic solids. *Applied Catalysis A: General* **2003,** *243* (1), 93-107.
44. Fridman, V.; Davydov, A., Dehydrogenation of cyclohexanol on copper-containing catalysts: I. The influence of the oxidation state of copper on the activity of copper sites. *Journal of Catalysis* **2000,** *195* (1), 20-30.
45. Beć, K. B.; Grabska, J.; Czarnecki, M. A., Spectra-structure correlations in NIR region: Spectroscopic and anharmonic DFT study of n-hexanol, cyclohexanol and phenol. *Spectrochimica Acta Part A: Molecular and Biomolecular Spectroscopy* **2018,** *197*, 176-184.
46. Tvaroska, I.; Carver, J. P., The anomeric and exo-anomeric effects of a hydroxyl group and the stereochemistry of the hemiacetal linkage11Ab Initio Molecular Orbital Calculation of Carbohydrate Model Compounds. Part 7. For Part 6, see ref[1]. *Carbohydrate Research* **1998,** *309* (1), 1-9.
47. Ghosh, A.; Jonnalgadda, P. N., Ab initio and DFT benchmark study for the calculations of isotopic shifts of fundamental frequencies for 2,3-dihydropyran. *Structural Chemistry* **2022,** *33* (3), 743-755.

48. Philip, T.; Cook, R. L.; Malloy, T. B., Jr.; Allinger, N. L.; Chang, S.; Yuh, Y., Molecular mechanics calculations and experimental studies of conformations of .delta.-valerolactone. *Journal of the American Chemical Society* **1981,** *103* (9), 2151-2156.
49. Chen, H.-Y.; Cheng, Y.-L.; Takahashi, K., Theoretical Calculation of the OH Vibrational Overtone Spectra of 1,5-Pentanediol and 1,6-Hexanediol. *The Journal of Physical Chemistry A* **2011,** *115* (50), 14315-14324.
50. Dorofeeva, O. V.; Suchkova, T. A., Theoretical calculation of enthalpy of formation of multiconformational molecules: 1,2-ethanediol, propanediols, and glycerol. *Chemical Physics Letters* **2018,** *698*, 218-222.
51. Lewis-Atwell, T.; Townsend, P. A.; Grayson, M. N., Comparisons of different force fields in conformational analysis and searching of organic molecules: A review. **2021,** *79*, 131865.
52. Yalamanchi, K. K.; Li, Y.; Wang, T.; Monge-Palacios, M.; Sarathy, S. M., Large-scale thermochemistry calculations for combustion models. *Applications in Energy and Combustion Science* **2022,** *12*, 100084.
53. Leitão, M. L. P.; Pilcher, G.; Meng-Yan, Y.; Brown, J. M.; Conn, A. D., Enthalpies of combustion of γ-butyrolactone, γ-valerolactone, and δ-valerolactone. **1990,** *22* (9), 885-891.